The Thesis Committee for Kanay Jerath
Certifies that this is the approved version of the following thesis:

RECONCILIATION OF TWO-DIMENSIONAL NMR MEASUREMENTS WITH THE PROCESS OF MUD-FILTRATE INVASION: SYNTHETIC AND FIELD EXAMPLES

APPROVED BY
SUPERVISING COMMITTEE:

Supervisor:

Carlos Torres-Verdín

Kishore K. Mohanty

RECONCILIATION OF TWO-DIMENSIONAL NMR MEASUREMENTS WITH THE PROCESS OF MUD-FILTRATE INVASION: SYNTHETIC AND FIELD EXAMPLES

by

Kanay Jerath, B.E.

Thesis

Presented to the Faculty of the Graduate School of

The University of Texas at Austin

in Partial Fulfillment

of the Requirements

for the Degree of

Master of Science in Engineering

The University of Texas at Austin

December 2011

Acknowledgements

I would like to thank The University of Texas at Austin's Research Consortium on Formation Evaluation, jointly sponsored by Anadarko, Apache, Aramco, Baker-Hughes, BG, BHP Billiton, BP, Chevron, ConocoPhillips, ENI, ExxonMobil, Halliburton, Hess, Maersk, Marathon Oil Corporation, Mexican Institute for Petroleum, Nexen, ONGC, Petrobras, Repsol, RWE, Schlumberger, Statoil, Total, and Weatherford for partially funding the work presented in the thesis.

I am thankful to my supervisor, Dr. Carlos Torres-Verdín, whose encouragement, guidance and support enabled me to develop a profound understanding of the concepts of formation evaluation. His inputs during the research and writing of this thesis were extremely helpful. He always led by example and I am thankful to him for encouraging me to be persistent and disciplined.

I would like to acknowledge Dr. Kishore K. Mohanty for his valuable comments and suggestions as the reader of this thesis.

Further, I would like to thank my friends for their support and help during my stay at The University of Texas at Austin. I wish to express my gratitude to the faculty and staff of the Department of Petroleum and Geosystems Engineering for their assistance throughout my stay as a student.

Finally, I wish to express profound gratitude toward my parents, Dr. Neelima Jerath and Mr. Vinod Kumar Jerath, and my brother Dr. Kinshuk Jerath for offering me unconditional love and support. Also, a special mention for Dr. Kinshuk Jerath and Dr. Smita Mukherjee for their contributions toward editing this thesis.

Abstract

RECONCILIATION OF TWO-DIMENSIONAL NMR MEASUREMENTS WITH THE PROCESS OF MUD-FILTRATE INVASION: SYNTHETIC AND FIELD EXAMPLES

Kanay Jerath, M.S.E.

The University of Texas at Austin, 2011

Supervisor: Carlos Torres-Verdín

Nuclear magnetic resonance (NMR) has become an effective borehole measurement option to assess petrophysical and fluid properties of porous and permeable rocks. In the case of fluid typing, two-dimensional (2D) NMR interpretation techniques have advantages over conventional one-dimensional (1D) interpretation as they provide additional discriminatory information about saturating fluids and their properties. However, often there is ambiguity as to whether fluids detected with NMR measurements are mobile or residual. In some instances, rapid vertical variations of rock properties (e.g. across thinly-bedded formations) can make it difficult to separate NMR fluid signatures from those due to pore-size distributions. There are also cases where conventional fluid identification methods based on resistivity and nuclear logs indicate dominant presence of water while NMR measurements indicate presence of water, hydrocarbon, and mud filtrate. In such cases, it is important to ascertain whether existing hydrocarbons are residual or mobile.

The radial lengths of investigation of resistivity, nuclear, and NMR measurements are very different, with NMR measurements being the shallowest sensing. Even in the case of several radial zones of NMR response attributed to different acquisition frequencies and DC magnetic field gradients, the measured signal originates from a fairly shallow radial zone compared to that of nuclear and resistivity logs. Depending on drilling mud being used and the radial extent of mud-filtrate invasion, the NMR response of virgin reservoir fluids can be masked by mud filtrate because of fluid displacement and mixing. In order to separate those effects, it is important to reconcile NMR measurements with electrical and nuclear logs for improved assessment of porosity and mobile hydrocarbon saturation.

Previously, Voss et al. (2009) and Gandhi et al. (2010) introduced the concept of Common Stratigraphic Framework (CSF) to construct and validate multi-layer static and dynamic petrophysical models based on the numerical simulation of well logs. In this thesis, the concept of CSF is implemented to reconcile 2D NMR interpretations with multi-layer static and dynamic petrophysical models. It is found that quantifying the exact radial zone of response and corresponding fluid saturations can only be accomplished with studies of mud-filtrate invasion that honor available resistivity and nuclear logs. This thesis indicates that the two interpretation methods complement each other and when applied in conjunction, improve and refine the overall petrophysical understanding of permeable rock formations.

Examples of successful application include field data acquired in thinly-bedded gas formations invaded with water-base mud, where bed-boundary effects are significant and residual hydrocarbon saturation is relatively high. In such cases, numerical simulation of mud-filtrate invasion and well logs acquired after invasion enables reliable interpretations of petrophysical and fluid properties. The interpretation procedure introduced in this thesis also provides an explicit way to determine the uncertainty of petrophysical and fluid interpretations.

Table of Contents

List of Tables

List of Figures

Chapter 1: Introduction

1.1 INTRODUCTION

Borehole NMR measurements have been extensively used in formation evaluation, and their effectiveness has improved substantially in the last decade. Modern borehole NMR tools are capable of acquiring a large number of echo-decay sequences when sampling magnetization decay and can control many acquisition parameters such as wait time (*TW*), inter-echo time (*TE*), number of echoes (*NE*), magnetic field gradient (*G*), etc. A unique combination of all these acquisition parameters can be selected, depending on the nature of fluids, to enhance polarization, relaxation, and diffusion of mobile hydrogen molecules in formation fluids. When processed together, measurements can yield valuable information including, but not limited to porosity, in-situ fluid type, and fluid saturations, among others.

Conventional interpretation techniques for NMR data yield a one-dimensional (1D) T_2 spectrum. It is very common to encounter different fluids in a reservoir with overlapping T_2 distributions. Such a behavior makes fluid typing ambiguous and inaccurate with 1D T_2 spectra. To circumvent this problem, it is advisable to add additional degrees of freedom to the acquisition and sampling of NMR data, thereby improving the diagnosis and assessment of saturating fluids (Sun and Dunn, 2005). Two-dimensional (2D) data acquisition has been found to be more beneficial than 1D acquisition because it can distinguish between fluids based on the contrast between two fluid properties instead of only one. Parameter selection for acquisition depends on reservoir fluid types (gas, oil, water and/or mud filtrate) and fluid properties (Chen et al., 2009).

Inversion of NMR data in two dimensions is a linear least-squares minimization problem and is very similar in theory to 1D inversion. However, compared to 1D inversion, 2D numerical algorithms are more complex because one must incorporate the effects of various measurement-acquisition parameters such as wait time (*TW*), inter-echo time (*TE*), number of echoes (*NE*), magnetic field gradient (*G*), etc.

An important objective of this thesis is the accurate and reliable identification of fluids and quantification of fluid saturations in invaded formations. In most cases, field data have very low signal to noise ratio (20-50 dB), which makes it necessary to construct algorithms that are robust in the presence of noise.

The radial length of investigation of borehole NMR measurements is short (approximately 6-10 in), which makes them very shallow sensing. This property indicates that petrophysical properties interpreted from NMR measurements originate from a shallow radial zone and, in most cases, are affected by the phenomena of mud-filtrate invasion, fluid displacement, and salt mixing. Depending on drilling fluids and the radial extent of invasion, virgin reservoir fluids will be displaced away from the wellbore and their NMR response will be masked by that of invading fluids. Therefore, fluid saturations calculated with NMR data in the presence of mud-filtrate invasion will be different from original in-situ fluid saturations. It is extremely important to isolate the effects of mud-filtrate invasion on NMR measurements for accurate and reliable petrophysical interpretation of rock formations. This can be accomplished by reconciling NMR measurements with electrical and nuclear logs.

Fluid typing and saturation calculations performed with NMR data can be ambiguous because it is challenging to ascertain whether the hydrocarbon component in the identified fluids is residual or mobile. This problem is aggravated in heterogeneous formations such as those exhibiting thin beds and high variability of petrophysical properties. An alternative for reliable interpretation of those complex cases is to construct multi-layer static and dynamic petrophysical models based on the numerical simulation of well logs. This is accomplished by implementing the concept of Common Stratigraphic Framework (CSF) with the software UTAPWeLS[1]. In doing so, numerical simulation of the process of mud-filtrate invasion is performed to describe the radial distributions of water saturation and salt concentration into invaded formations. Such simulations yield the radial distribution of displaced hydrocarbons and connate water from which one can determine whether hydrocarbon observed at the radial zone coinciding with the radial length of investigation of NMR measurements is mobile or residual.

In thinly-bedded formations, bed-boundary effects on well logs are significant, resulting in biased interpretations because conventional well-log interpretation methods do not account for these effects. One of the most important conclusions of the present study is that reliable petrophysical interpretation requires the assessment of the radial zone of response of NMR measurements together with the radial distribution of fluid saturation. To that end, numerical simulation of the process of mud-filtrate invasion must be performed to honor available apparent resistivity and nuclear logs. One way to accomplish that objective is to implement the CSF concept to construct multi-layer static and dynamic models and reconcile 2D NMR interpretations with them. The two interpretation methods complement each other and improve the petrophysical assessment of permeable formations.

[1] Developed by The University of Texas at Austin's Research Consortium on Formation Evaluation.

1.2 T_1, T_2 AND 2D NMR FUNDAMENTALS

There are two characteristic magnetic relaxation times of fluids in porous media: transverse relaxation time, T_2, and longitudinal relaxation time, T_1. The analytical expression for T_1 is described by

$$\frac{1}{T_1} = \frac{1}{T_{1B}} + \rho_1 \frac{S}{V}, \tag{1.1}$$

where T_{1B} is bulk fluid longitudinal relaxation time. Surface relaxation occurs at the fluid-solid interface where ρ_1 corresponds to T_1 surface relaxivity, and S/V is the ratio of pore surface to pore volume. For a typical Carr-Purcell-Meiboom-Gill (CPMG) echo sequence, the analytical expression for T_2 is given by

$$\frac{1}{T_2} = \frac{1}{T_{2B}} + \rho_2 \frac{S}{V} + \frac{\left(\gamma \cdot G \cdot TE\right)^2 \cdot D}{12}, \tag{1.2}$$

where T_{2B} is the intrinsic or fluid bulk transverse relaxation time, and ρ_2 is the T_2 surface relaxivity (Fukushima and Roeder, 1981). Additionally, γ is gyromagnetic ratio for a hydrogen proton, G is the average magnitude of the DC magnetic field gradient over the entire sample, TE is inter-echo spacing in the CPMG sequence, and D is effective fluid diffusivity. Relaxivity of the surface between two fluid phases is negligible; however, that between a fluid phase and rock can have diverse values depending on rock/fluid pairs (Kenyon, 1997).

Wait time, TW, is the time for T_1 polarization, allowing magnetization to build up when polarizing existing hydrogen protons. Inter-echo time, TE, is the interval between two CPMG pulses; TW and TE are the two main parameters controlling measurements and inversion of T_1 and T_2 spectra. Implementing a range of values for these two parameters while acquiring NMR data helps to reduce the non-uniqueness of NMR interpretations. Measurements and inversion algorithms based on the variation of only one acquisition parameter may exhibit high non-uniqueness. Performing inversion in two dimensions adds another degree of freedom to identify fluids based on the contrast of T_{2B} and T_{1B}, or T_{2B} and D, for in-situ fluids.

1.3 Motivation and Problem Statement

In many cases, conventional 1D NMR fluid typing and interpretation do not have sufficient degrees of freedom for accurate and unique quantitative evaluation. For example, in heavy oil, the T_{2B} relaxation time of hydrocarbon is usually very short and overlaps with the T_{2B} components of capillary-bound and clay-bound water, making them indistinguishable. Also, calculations of partial porosity and saturation for each fluid can be highly non-unique. Two-dimensional NMR logging techniques are particularly useful in such cases because fluid typing becomes less uncertain with 2D maps as they enhance fluid signatures. This concept is explained graphically in **Figures 1.1** and **1.2**. **Figure 1.1** describes a synthetic, 1D NMR T_2 distribution in solid blue, which is the superposition of the 1D NMR T_2 distributions of two different synthetic reservoir fluids, shown in dashed blue lines. Conventional 1D interpretation indicates a single peak, which is incorrectly interpreted as the presence of a single fluid. However, when the same data are processed using 2D algorithms, as described in **Figure 1.2**, two distinct fluid signatures emerge because of their differences in fluid diffusivity.

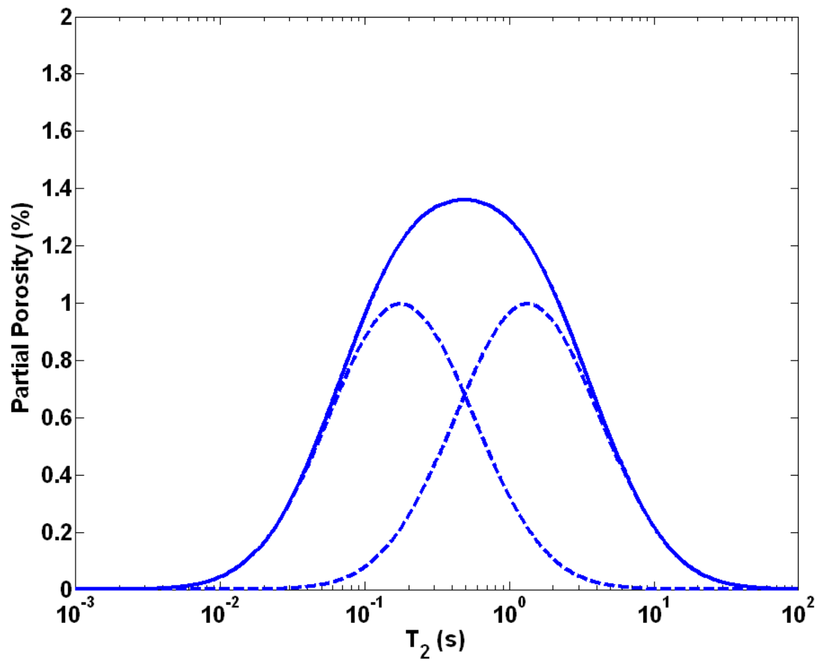

Figure 1.1: Conventional 1D NMR interpretation method used to generate T_2 distributions. The solid blue line identifies the composite T_2 distribution, which is a superposition of the individual T_2 distribution of two different fluids, here identified with dashed blue lines.

The first objective of this thesis is to develop an algorithm for linear inversion of NMR data in two dimensions, namely T_1-T_2 or T_2-D, to obtain 2D NMR maps. Such 2D maps render a distribution of partial porosity of the various fluids included in the pore space. The algorithm involves three major steps, which are explained in detail in Section 2.1 of the thesis. From these 2D maps, numerical calculations can be performed to quantify total porosity, partial porosity, and relative saturation of each fluid component. Quantification of partial porosity with 2D maps is more accurate than conventional 1D interpretation because each fluid exhibits a distinct signature which allows better quantification of its individual contribution to total porosity. Porosity uncertainty due to noisy measurements can also be calculated as a byproduct of 2D NMR map estimation.

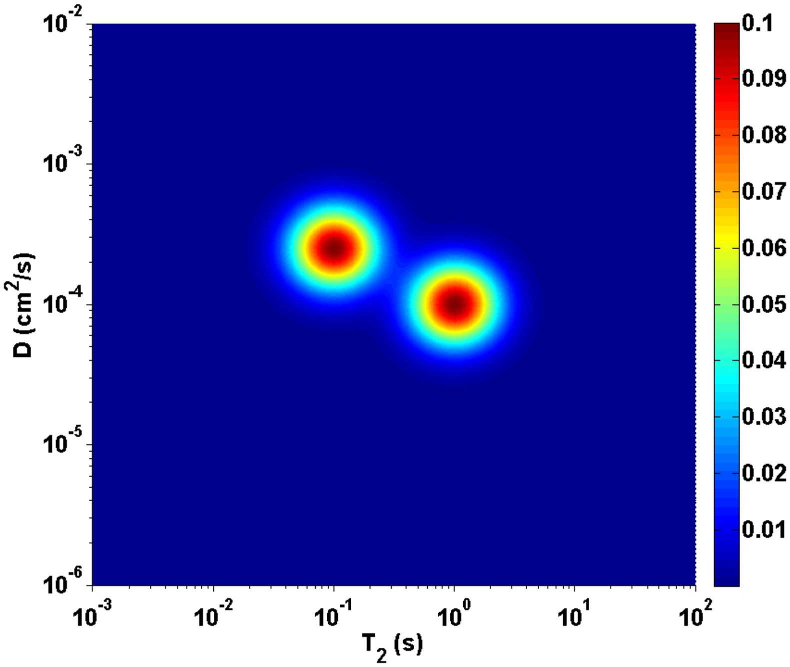

Figure 1.2: T_2-D map obtained after 2D inversion of NMR data distinctly showing the two fluid signatures because of their contrast in fluid diffusivity. The color bar to the right describes porosity in percentage.

It is important to emphasize that NMR measurements have a very short radial length of investigation, whereby they are inevitably influenced by the processes of mud-filtrate invasion, fluid displacement, and salt mixing. A 2D map obtained from these measurements is associated with a very narrow and shallow radial window into the examined formation after mud-filtrate invasion, fluid mixing, and displacement have taken place. This behavior indicates that fluid signatures observed on 2D NMR maps do not always represent virgin reservoir fluids because they have been partially displaced by mud filtrate. Consequently, there is ambiguity as to whether fluids diagnosed with NMR interpretations are mobile or irreducible. An understanding of the radial distribution of fluid saturation is necessary to solve this problem. It was found that simulation of the process of mud-filtrate invasion in combination with other wireline measurements such as resistivity and nuclear logs, improves the diagnosis and appraisal of fluids and enables the differentiation of mobile and residual fluids. The central objective of this thesis is to develop an interpretation method that effectively combines 2D NMR data and the physics of mud-filtrate invasion to detect and quantify reservoir fluids and their saturations.

1.4 OUTLINE OF THE THESIS

Chapter 2 of the thesis discusses the method implemented to obtain T_1-T_2 and T_2-D maps, including formulation of the forward and inverse problems. Thereafter, a synthetic case is discussed in Chapter 3. In Chapters 4, 5 and 6, three field cases are introduced to examine the combined interpretation of NMR inversion results with static and dynamic properties obtained with the CSF. This latter step involves construction of multi-layer static and dynamic petrophysical models based on the numerical simulation of well logs. Finally, Chapter 7 summarizes and discusses the conclusions stemming from the study.

Chapter 2: Method

In keeping with the objectives of the thesis, interpretation methods introduced are divided in the following way:

(1) Development of an algorithm for two-dimensional inversion of NMR data, and

(2) Construction of multi-layer static and dynamic petrophysical models based on numerical simulation of well logs and their combination with 2D maps NMR maps.

This chapter describes the development of the algorithm for 2D inversion of NMR data.

2.1 Inversion of NMR Data in Two Dimensions

The physics of NMR signals measured with the CPMG spin echo method indicates that one can relate a model, *m,* to the observations or data acquired, *d,* using a function, *F*, given by

$$F(m) = d\ . \tag{2.1}$$

NMR relaxation measurements, whether transverse (T_2), longitudinal (T_1) or diffusion based (D), can be expressed as a multi-exponential time-decay function. However, the interpretation of NMR measurements is an inverse problem because one seeks to transform the data (magnetization time decay measurements acquired with the NMR tool) to partial porosity space (2D partial porosity map for in-situ fluids). Given that model and data are both functions of time, the estimation is classified as a continuous inverse problem. To solve a continuous inverse problem numerically, the function F must be discretized within defined numerical intervals, namely partial porosity obtained within T_2-T_1 or T_2-D maps.

For a continuous linear inverse problem, F can be expressed as a linear integral operator. Because the unknown function is two-dimensional, the forward problem described by equation (2.1) can be expressed as

$$\int_{y1}^{y2}\int_{x1}^{x2} f(s_k; x, y)\cdot m(x, y)\cdot dx\ dy = d(s_k)\ , \tag{2.2}$$

where the function $f(s_k;x,y)$ is called the kernel, $m(x,y)$ denotes the unknown 2D model of independent variables x and y, d represents the data and x_1, x_2, and y_1, y_2 represent the integration limits in the x and y dimensions, respectively. The objective is to estimate $m(x,y)$ from noisy and discrete measurements. Equations of this form are classified as Fredholm integral equations of the first kind (IFKs) (Aster et al., 2005) and they arise in a large number of inverse problems. The function $f(s_k;x,y)$ in equation (2.2) is discretized with pulse basis functions (Aster et al., 2005), expressed by the equation

$$\sum_{i=1}^{N}\sum_{j=1}^{M} f_{ij}(s_k)\cdot\left[\int_{\Delta i}\int_{\Delta j} m(x, y)\cdot dx\ dy\right] = \ d(s_k)\ ,\ m(x, y)\geq 0\,, \tag{2.3}$$

where, for the case of NMR measurements, f_{ij} represents a discrete element of the 2D kernel, $m(x,y)$, which is also referred to as a 2D porosity distribution function, represents non-negative partial porosity of fluids, and d represents the acquired data; $m(x,y)$ is also referred to as a 2D porosity density function. The pulse basis function is explained in further detail in section 2.1.2 of this thesis.

Linear inversion techniques are applied to estimate continuous partial porosity distribution maps, *m(x,y)*, in two dimensions using constrained least-squares minimization. The three basic steps which constitute the linear inversion method are summarized in the following sections. A discretized form of equation (2.3) can be expressed as the matrix product

$$\boldsymbol{F} \cdot \boldsymbol{m} = \boldsymbol{d}, \tag{2.4}$$

where $\boldsymbol{F}$ is the discretized representation of the kernel, $\boldsymbol{m}$ is the discretized representation of the two-dimensional model, *m(x,y)*, and $\boldsymbol{d}$ represents the data vector. Accordingly, the multi-exponential function which relates the function *F*, and the model, *m*, to the data, *d*, is described by

$$\begin{aligned} d(t,TW,G) &= \sum_{j}^{J}\sum_{i}^{I} m_{i,j}\left(1-e^{-\frac{TW}{R\cdot T_{2,i}}}\right)\cdot e^{-\frac{t}{T_{2,i}}-\frac{D_j (TE\cdot G\cdot \gamma)^2 t}{12}} \\ m_{i,j} &= \int_{\Delta i}\int_{\Delta j} m(x,y)\cdot dx\ dy \end{aligned}, \tag{2.5}$$

where $m_{i,j}$ represents the partial porosity at a certain point on the 2D grid, *TW* is wait time, T_2 is transverse relaxation, *D* is fluid diffusivity, *TE* is inter-echo time, *G* is magnetic field gradient, γ is the gyromagnetic ratio for a hydrogen proton, *R* is the ratio of T_1 and T_2, and *t* is time. Index *i* designates the discrete range of values for T_2, and *j* designates the discrete range of values for fluid diffusivity (Chen et al., 2009). The value of *R* remains constant for a specific data acquisition sequence. For example, if the NMR data are being acquired in a water-bearing interval, it is generally fixed at 1, while in a hydrocarbon-bearing interval, it is greater than 1; for gas zones, *R* can be as high as 10. Reliable acquisition and interpretation of NMR data suggests that the value of *R* should be calculated experimentally from in-situ fluid samples to secure sufficient sensitivity to D in the data.

2.1.1 Data Compression

Data compression is aimed at decreasing the number of data points which have to be used in the estimation of 2D NMR maps representing partial porosity. As mentioned earlier, NMR tools use a CPMG pulse sequence to generate a spin-echo train. The new generation of NMR tools have the ability to produce a very large number of pulses in a single spin-echo train, typically a thousand pulses or even more. Moreover, with these tools, multiple spin-echo trains can be generated at each sampling interval, often as many as 25. All these data, when synthesized, carry a significant amount of information which is difficult to process in real time. Consequently, data compression is needed prior to performing the estimation of 2D NMR maps.

Decay sequences acquired for every echo-train are individually compressed into smaller windows. The compression algorithm is designed to provide flexibility when choosing the desired compression for a given decay sequence (Dunn and LaTorraca, 1999). **Figure 2.1** shows a typical exponentially decaying spin-echo train where data were acquired under noisy field conditions and consisted of 1000 pulses (i.e. NE is 1000).

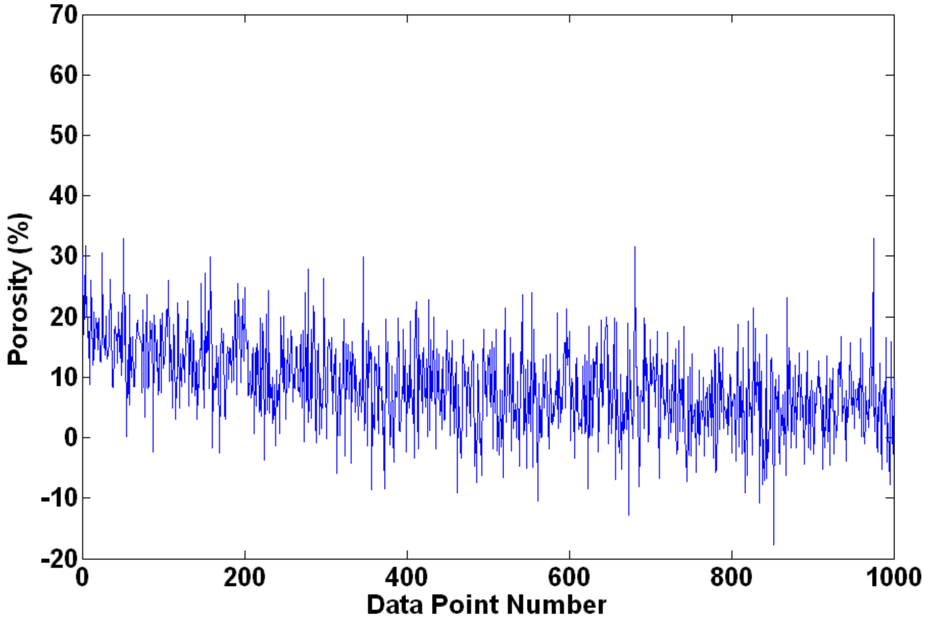

Figure 2.1: Example of measured NMR echo-decay train consisting of 1000 data points (*NE* = 1000). Data are noisy and have a low SNR. The echo-decay train is reduced to a smaller number of data points with a compression algorithm.

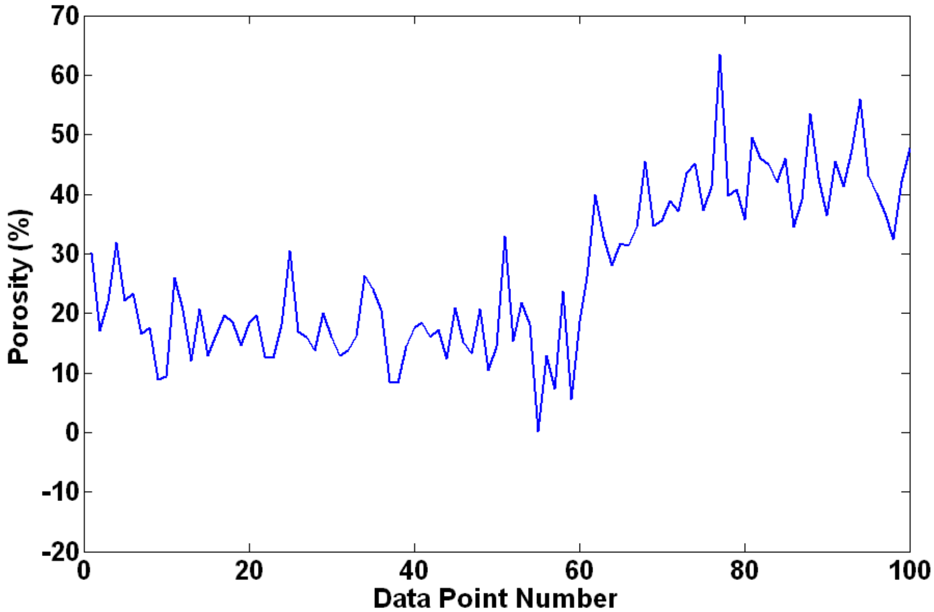

Figure 2.2: The echo-decay train shown in **Figure 2.1** was reduced to 100 data points (*NE* = 100) using a compression algorithm. Because the compression algorithm uses a variable window size in the time domain, the echo-decay train loses its typical shape of an exponential decay. This behavior is explained in detail in the text.

As shown in **Figure 2.2**, echo-decay trains can be compressed into smaller data samples. Data shown in **Figure 2.2** do not resemble a decay sequence after compression, especially during late times, because of the variable moving window size used by the compression algorithm to reduce the number of data points. NMR decay signals embody the most important information during early times and generally asymptote to zero during late times, where signal amplitude gradually becomes negligible. The compression algorithm is designed to use a small compression window at early times whereas at late times it uses a much longer window. This strategy emphasizes the important early-time information, while reducing large segments of the late-time data into much fewer data points. Additionally, data compression ensures shorter CPU times without being detrimental to the estimation of 2D NMR partial porosity maps.

2.1.2 Discretization of the Kernel

As mentioned in the introduction of Section 2.1, a standard discretization procedure is implemented with pulse basis functions which postulate a piecewise constant approximation for the unknown model *m*, and provide the basis for a matrix formulation of an equivalent discrete inverse problem (Aster et al., 2005). The discretized version of kernel, $\boldsymbol{F}$, can be expressed as

$$\boldsymbol{F} = \begin{bmatrix} \boldsymbol{F}_1 \\ \boldsymbol{F}_2 \\ \vdots \\ \boldsymbol{F}_k \\ \vdots \\ \boldsymbol{F}_K \end{bmatrix}_{K\cdot NE,\, I\cdot J} \tag{2.6}$$

,

$$\boldsymbol{F}_k = \begin{bmatrix} f_{1,1}^{k} & \cdots & f_{1,I\cdot J}^{k} \\ \vdots & \ddots & \vdots \\ f_{NE,1}^{k} & \cdots & f_{1,I\cdot J}^{k} \end{bmatrix}_{NE,\, I\cdot J}$$

where the entries $f_{i,j}^{k}$ are given by

$$f_{i,j}^{k} = \left(1 - e^{-\frac{TW_k}{R\cdot T_{2,j}}}\right) \cdot e^{-\frac{t_i}{T_{2,j}} - \frac{D_j (TE_k \cdot G_k \cdot \gamma)^2 t_i}{12}} . \tag{2.7}$$

In equation (2.7), k designates values of respective acquisition parameters for the k^{th} echo-decay sequence (out of a total of K sequences) while i and j designate discrete values for T_2 and D, respectively.

Data vector $\boldsymbol{d}$ designates the data acquired by the NMR tool during the suites of time-decay measurements, concatenated to construct a composite data vector given by

$$\boldsymbol{d} = \left[d_1^1, d_2^1, \cdots, d_{NE}^1, \ \cdots, d_1^k, d_2^k, \cdots, d_{NE}^k, \ \cdots, d_1^K, d_2^K, \cdots, d_{NE}^K \right]_{1, K \cdot NE}^T \tag{2.8}$$

,

where d_i^k designates the i^{th} time sample acquired during the k^{th} echo-decay sequence out of a total of K time-decay sequences acquired, and "T" represents the transpose operator. Therefore, $\boldsymbol{m}$ takes the form

$$\boldsymbol{m} = \left[m_{1,1}, \ m_{1,2}, \cdots, m_{1,j}, m_{2,1}, \ m_{2,2}, \cdots, m_{2,j}, \cdots, m_{i,1}, \ m_{i,2}, \cdots, m_{i,j} \right]_{1, I \cdot J}^T \tag{2.9}$$

,

where m_{ij} represents a partial porosity value on the 2D NMR map, as described in equation (2.5). Although $\boldsymbol{m}$ represents partial porosity values for a 2D grid, it is estimated in the form of a vector to be subsequently arranged in the form of a 2D grid. For all the examples discussed in this thesis, discretization was performed by maintaining uniform logarithmic grid spacing (log-10 base) for the variables representing partial porosity, such as T_1, T_2, or D, with 10 samples per decade, within the lower and upper bounds of 10^{-4} s $\leq T_1 \leq 10$ s; 10^{-4} s $\leq T_2 \leq 10$ s; and 10^{-6} cm^2/s $\leq D \leq 10^{-2}$ cm^2/s.

2.1.3 Regularization and Smoothing

The inverse problem can be formulated as the constrained minimization of the quadratic cost function

$$C(\boldsymbol{m}) = \left\| \boldsymbol{W_d} \cdot (\boldsymbol{F} \cdot \boldsymbol{m} - \boldsymbol{d}) \right\|_2^2 + \lambda^2 \left\| \boldsymbol{W_m} \cdot \boldsymbol{m} \right\|_2^2 \ , \ m_{ij} \geq 0 \, , \tag{2.10}$$

where $\boldsymbol{W_d}$ is a data weighting matrix, $\boldsymbol{W_m}$ is a model weighting matrix, and λ is a regularization (stabilization) parameter. Because of the decaying exponential nature of the kernel $\boldsymbol{F}$, small perturbations in the data may manifest as large changes in inversion results, implying that the estimation is an ill-posed problem. To overcome this difficulty, a penalty function is added to the cost function with a regularization (stabilization) constant λ (Aster et al., 2005). The purpose of the regularization constant is to stabilize the estimation method by choosing an optimal weight for the additive components of the quadratic cost function. By doing so, a regularized solution is obtained which honors the measurements without exhibiting irregular oscillations due to noisy and/or inadequate data. For this study, Hansen's L-curve method was implemented to select the regularization constant (Hansen, 2007), which has been found to be effective in yielding stable and robust estimations of $\boldsymbol{m}$, even in the presence of noisy borehole NMR measurements with low SNR.

In equation (2.10), $\boldsymbol{W_d}$ is a diagonal matrix calculated from the standard deviation of noise associated with each spin-echo train via the equation

$$\begin{gathered}\boldsymbol{W_d} = \boldsymbol{\sigma}_{\boldsymbol{noise}}^{-1} \cdot \boldsymbol{I}_{K\cdot NE,K\cdot NE} \\ \boldsymbol{\sigma_{noise}} = \left[\sigma_{noise,1} \;\vdots\; \sigma_{noise,2} \;\vdots\; \cdots \;\vdots\; \sigma_{noise,k} \;\vdots\; \cdots \;\vdots\; \sigma_{noise,K} \right]^T_{1,K\cdot NE}\end{gathered}, \tag{2.11}$$

where $\sigma_{noise,k}$ represents the standard deviation of noise associated with the k^{th} spin-echo train and $\boldsymbol{I}$ represents the identity matrix. Matrix $\boldsymbol{W_d}$ is used to attach specific weights to each echo-decay sequence. For example, if a measured echo-decay sequence is very noisy, it can be assigned a small weight, compared to less noisy measurements. By doing so, the inversion algorithm is biased to perform a better fit to the more reliable measurements. Additionally, $\boldsymbol{W_m}$ is the discrete version of a first-order, stabilizing matrix given by

$$\boldsymbol{W_m} = \begin{bmatrix} -1 & 1 & & & & \\ & -1 & 1 & & & \\ & & \ddots & \ddots & & \\ & & & -1 & 1 & \\ & & & & -1 & 1 \end{bmatrix}_{I\cdot J, I\cdot J} . \tag{2.12}$$

2.2 CONSTRUCTION OF STATIC AND DYNAMIC MULTI-LAYER RESERVOIR MODELS

Static and dynamic multi-layer models were constructed to incorporate the process of mud-filtrate invasion in the calculation of in-situ gas saturation. Accordingly, a CSF was constructed using the software UTAPWeLS[2] to simulate different radial invasion profiles in the analysis. Numerical simulation of the process of mud-filtrate invasion was performed to calculate radial distributions of water saturation and salt concentration into the invaded formations. Simulations were conditioned by drilling variables such as type of mud, time of invasion, and overbalance pressure. They also included layer-by-layer values of porosity, permeability, capillary pressure, and relative permeability, some of which were defined based on available core data. Finally, simulations included fluid properties such as density, viscosity, salt concentration of mud-filtrate, salt concentration of connate water, and temperature. Subsequently, numerically simulated radial distributions of water saturation were transformed into radial distributions of electrical resistivity (using Archie's equation with values of variables *a*, *m*, and *n* obtained from core analysis), density, and migration length, to

[2] Developed by The University of Texas at Austin's Research Consortium on Formation Evaluation.

numerically simulate the corresponding apparent resistivity, density, and neutron porosity logs.

Figure 2.3 describes the CSF used to construct multi-layer reservoir models. It is an iterative process where the mismatch between well logs and their numerical simulations is progressively reduced by adjusting layer-by-layer petrophysical properties. Initial reservoir properties, i.e. absolute permeability, porosity, relative permeability, capillary pressure, and water saturation, are calculated from conventional petrophysical interpretation of well logs and available core measurements. For formations where core data are not available, the initial guess for petrophysical properties was constructed from previously-defined rock types whose core measurements were available in a different section of the well. Mud-filtrate invasion was numerically simulated using those formation properties. Available well logs were then compared to the corresponding numerically simulated logs. Depending on the degree of mismatch between measured well logs and their numerical simulations, progressive adjustments were made to layer-by-layer petrophysical properties until reaching an acceptable agreement.

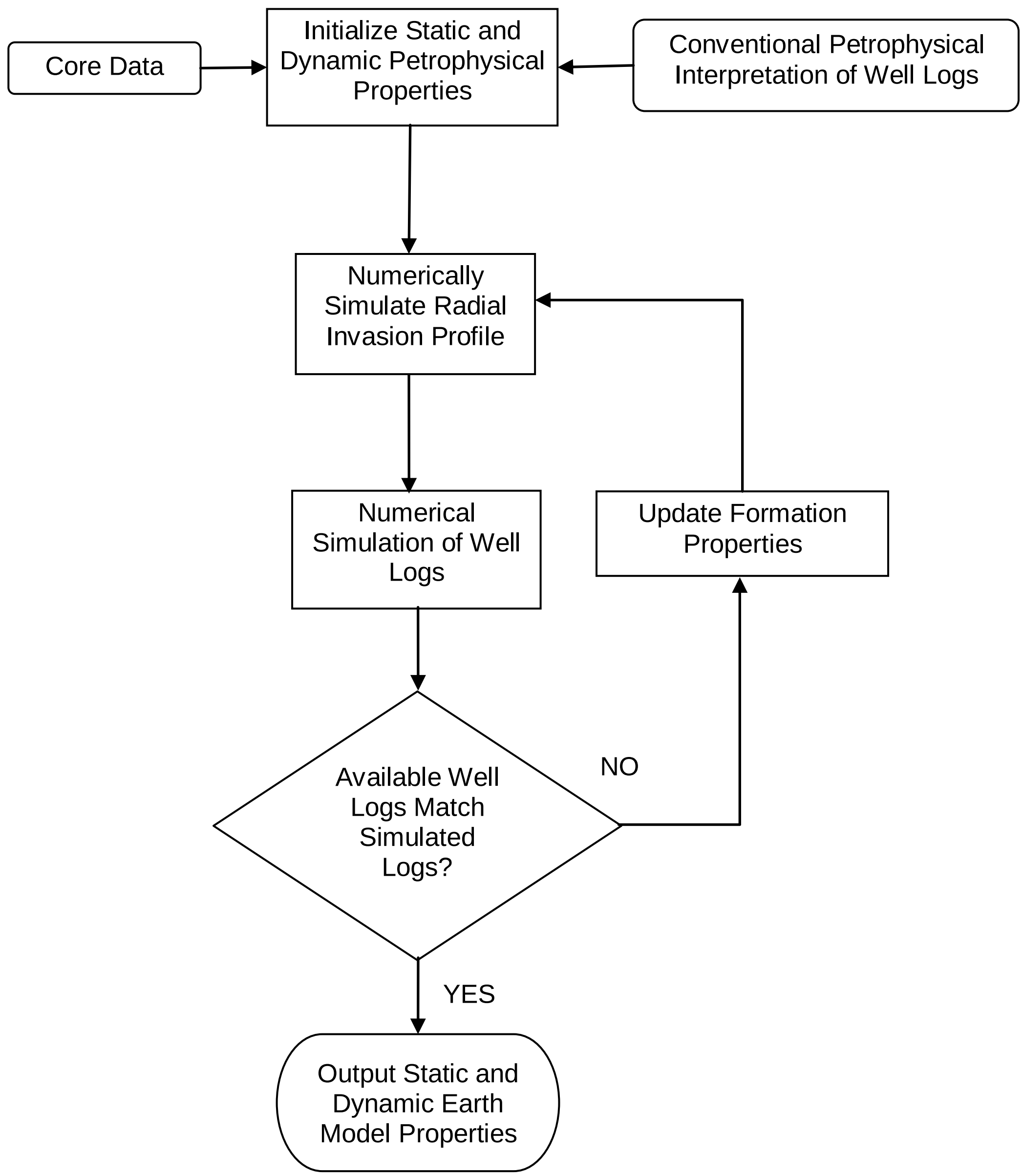

Figure 2.3: Flow chart describing the iterative method adopted in this thesis to reduce the mismatch between resistivity and nuclear logs and their numerical simulations. This process yields static and dynamic multi-layer reservoir models that honor all the available measurements and the physics of mud-filtrate invasion.

Numerical simulation of the process of mud-filtrate invasion enables the verification of consistency of well logs because of differences in vertical resolution and radial length of investigation. A pertinent example is that NMR, density, and resistivity logs are often incompatible because their volumes of investigation do not include the same spatial distribution of fluid saturation when the formation has been from moderately to deeply invaded with mud filtrate (Voss et al., 2009). Reconciliation of petrophysical interpretations performed with NMR measurements with those performed with the CSF helps to improve the reliability and accuracy of estimated petrophysical properties.

Chapter 3: Synthetic Case

This chapter introduces a synthetic case intended to appraise the reliability and accuracy of linear inversion when estimating 2D porosity maps from numerically simulated NMR data. Subsequently, synthetic Gaussian noise is added to the data to quantify uncertainty of 2D inversion results and to verify the robustness of the inversion algorithm.

3.1 Synthetic Case No. 1

In this synthetic case, T_2 and D are selected as the discretization variables. Four reservoir fluids, namely free water, irreducible water, light oil, and heavy oil were assumed to generate the synthetic data via the equation

$$d(t,G,TE) = \sum_i^I \sum_j^J m_{i,j} \cdot e^{-\frac{t}{T_{2,i}} - \frac{D_j (TE \cdot G \cdot \gamma)^2 t}{12}}, \tag{3.1}$$

where d are the data, $m_{i,j}$ represents the partial porosity at a certain point on the 2D grid, T_2 is transverse relaxation, D is fluid diffusivity, TE is inter-echo time, G is magnetic field gradient, γ is the gyromagnetic ratio for a hydrogen proton, and t is time. The indices I and J define the number of discretized values of m in the T_2 and D domains, respectively.

As shown in **Table 3.1**, synthetic data were simulated using discrete values of T_2 and D for each fluid. Ten spin-echo decay trains were generated, with each spin-echo train comprising 2000 echoes (NE) and a unique value of TE. For each spin-echo train, these 2000 data points were reduced to 64 data points using the compression algorithm.

Table 3.2 describes other pertinent properties used to generate the synthetic data. To verify the robustness of the inversion algorithm, 5% normally distributed Gaussian noise was added to the synthetic data.

Fluid	***T_2* [s]**	***D* [cm^2/s]**
Free Water	1	5×10^{-5}
Light Oil	0.1	5×10^{-6}
Irreducible Water	0.01	5×10^{-5}
Heavy Oil	0.01	5×10^{-7}

Table 3.1: Synthetic Case No. 1: Values of T_2 and D for fluids assumed in the numerical simulation of synthetic NMR measurements.

Parameter	**Symbol**	**Units**	**Value(s)**
Inter-Echo Time	*TE*	ms	0.1 , 0.5 , 1 , 3 , 5 , 7 , 10 , 20 , 50 , 100
Number of Echoes	*NE*	[]	2000
Magnetic Field Gradient	*G*	gauss/cm	10

Table 3.2: Synthetic Case No. 1: Data acquisition parameters assumed in the simulation of synthetic NMR data.

Figure 3.1 shows the T_2-D map estimated from the synthetic data. For generating this result, data weighting ($\boldsymbol{W_d}$) and model weighting ($\boldsymbol{W_m}$) matrices were assumed to be equal to the identity matrix, $\boldsymbol{I}$. Four distinct fluid signatures can be identified from the estimated T_2-D map. **Table 3.1** lists the values for T_2 and D used to simulate the synthetic data. The peaks of the 2D map shown in **Figure 3.1** agree very well with the input T_2 and D values. Using unity data and model-weighting matrices renders a 2D map which does not exhibit sufficient smoothing. This behavior is attributed to the fact that the synthetic data were created with discrete values of T_2 and D for each fluid instead of those of continuous distributions. Conventional 1D interpretation of the same synthetic data would yield the T_2 response shown in the T_2 projection panel. It is observed that the T_2 projection exhibits only three peaks, which would wrongly lead one to believe that the formation includes only three fluids. This behavior is due to the fact that the bulk transverse relaxation times, T_{2B}, for irreducible water and heavy oil are very close. However, due to the contrast in effective diffusivity of irreducible water and heavy oil, four distinct fluid signatures are observed on the 2D map. This is wherein lies the advantage of 2D inversion of NMR data over conventional 1D interpretation methods.

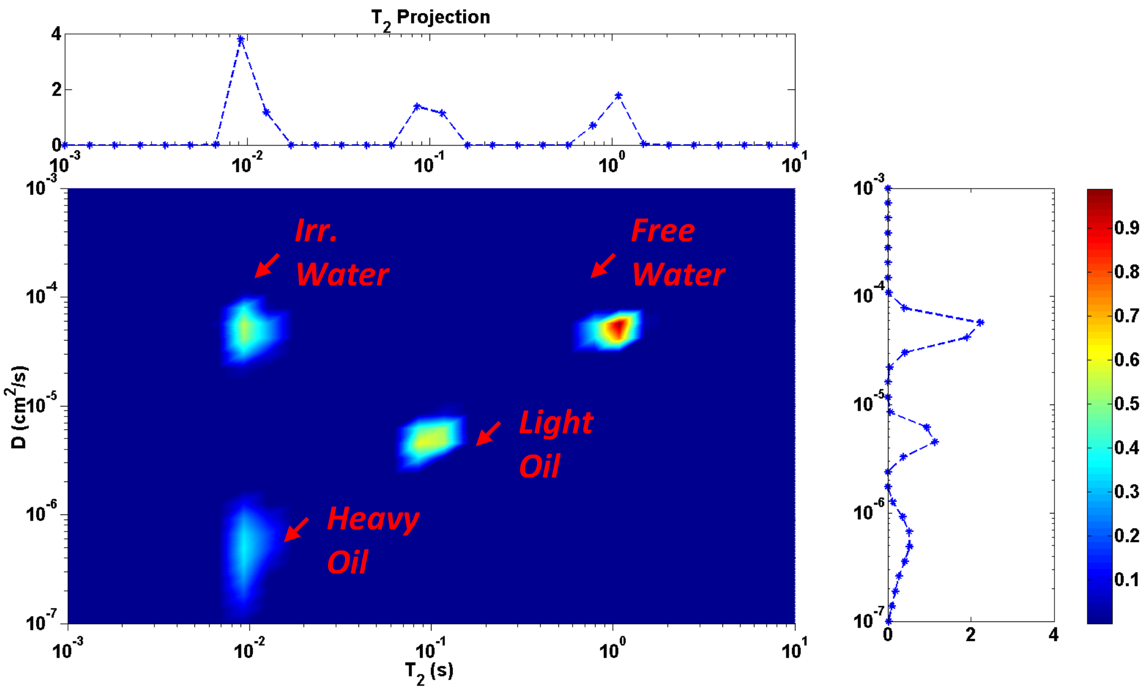

Figure 3.1: Synthetic Case No. 1: T_2-D map estimated from synthetic data showing four fluid signatures. Because data and model weighting matrices ($\boldsymbol{W_d}$ and $\boldsymbol{W_m}$, respectively) are equal to the identity matrix, the image does not exhibit sufficient smoothing. The color bar to the right describes porosity in percentage. Total porosity equal to 10% was assumed to generate the synthetic data.

Figure 3.2 shows the T_2-D map obtained from the same synthetic data but with the use of data weighting ($\boldsymbol{W_d}$) and model weighting ($\boldsymbol{W_m}$) matrices constructed as indicated in Section 2.1.3. In particular, matrix $\boldsymbol{W_d}$ was constructed by including the standard deviation of noise added to each spin-echo decay train, as described in equation (2.11). It is observed that the peaks for fluid signatures do not move but that the implementation of a non-unity model weighting matrix ($\boldsymbol{W_m}$) yields smoother (broader) signatures for all the fluids included in the 2D map, when compared to the result shown in **Figure 3.1**.

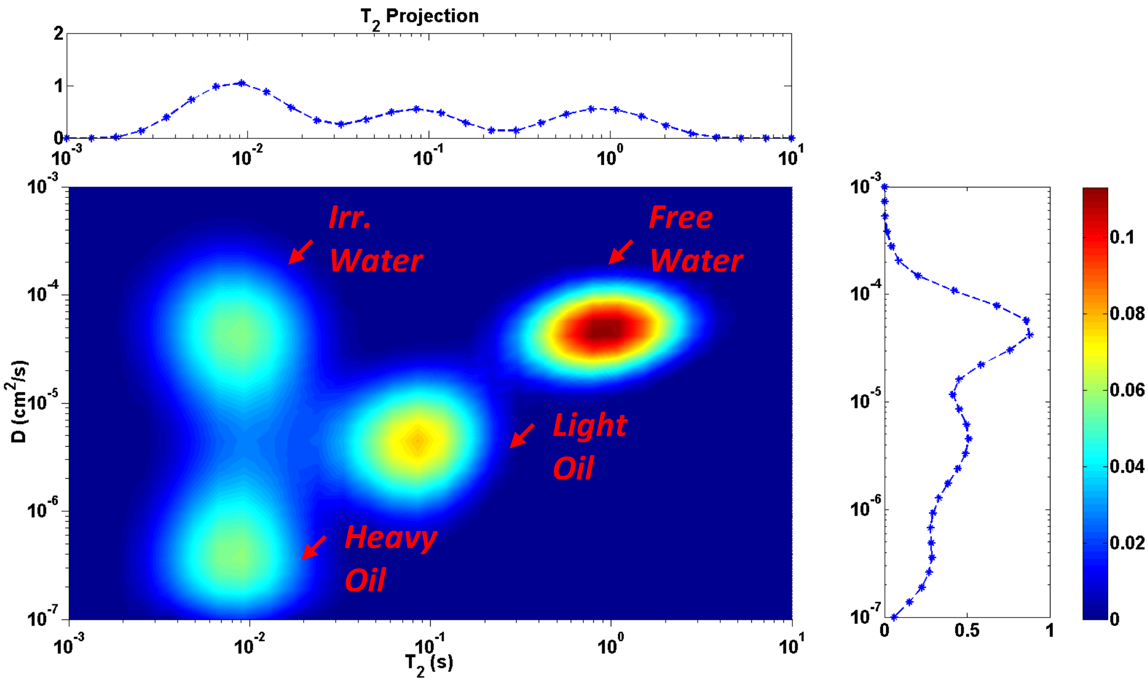

Figure 3.2: Synthetic Case No. 1: The same T_2-D map, described in **Figure 3.1**, is estimated using non-unity data and model weighting matrices ($\boldsymbol{W_d}$ and $\boldsymbol{W_m}$, respectively). Fluids exhibit smooth signatures compared to **Figure 3.1**. The color bar to the right describes porosity in percentage. Total porosity equal to 10% was assumed to generate the synthetic data.

To appraise the stability of inversion results, uncertainty analysis was performed for the estimated T_2-D map and the T_2 distribution. **Figures 3.3** and **3.4** describe the T_2-D uncertainty map and the T_2 uncertainty bars, respectively. Results were obtained by adding 5% normally distributed Gaussian random noise to the data. Uncertainty was quantified by calculating the standard deviation of errors at each measurement point. On the T_2-D uncertainty map, it is observed that uncertainty is maximum at fluid signature peaks as well as at locations between peaks. Similar behavior is observed with uncertainty bars for the T_2 distribution. Uncertainty bars are maximum at points of fast slope change, i.e. crests and troughs. It is also noted that uncertainty tends to be higher toward low values of T_2, in the vicinity of clay-bound and capillary-bound water signatures.

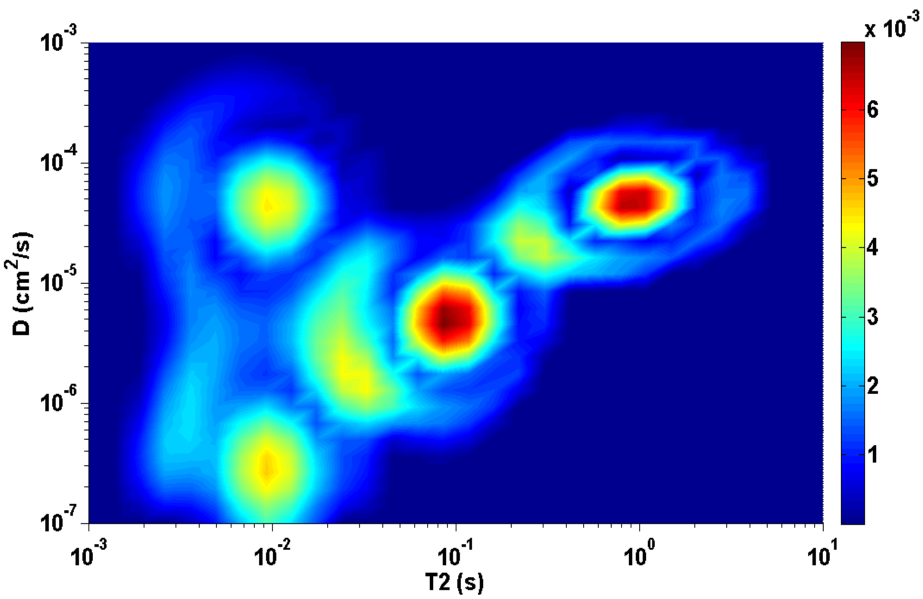

Figure 3.3: Synthetic Case No. 1: T_2-D uncertainty map calculated by adding 5% Gaussian synthetic noise to the data. Uncertainty is maximum at peaks and troughs of fluid signatures. The color bar to the right describes porosity in percentage.

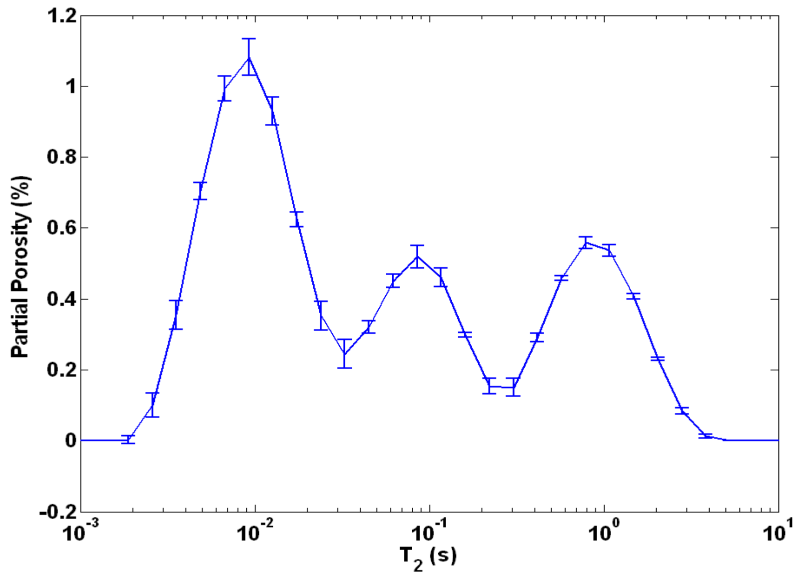

Figure 3.4: Synthetic Case No. 1: Uncertainty bars for the T_2 distribution estimated by adding 5% Gaussian synthetic noise to the data. Uncertainty is maximum at peaks and troughs.

An important observation is that, despite adding synthetic noise, locations of peaks for fluid signatures remain constant. No anomalous behavior is observed on the 2D map shown in **Figure 3.2** because of the addition of noise. This exercise verifies that the inversion algorithm is robust in the presence of noisy measurements.

Chapter 4: Field Case No. 1: Tight-Gas Siliciclastic Formation

This field case studied in this chapter is intended to:

(1) Appraise the reliability and accuracy of the 2D NMR inversion algorithm, and
(2) Reconcile NMR measurements with multi-layer static and dynamic petrophysical models constructed from the simulation of mud-filtrate invasion and well logs.

Available measurements include apparent resistivity logs, nuclear logs, and NMR measurements, as well as core measurements of porosity and permeability within some selected depth intervals. It was found that well logs were influenced by the process of mud-filtrate invasion, especially NMR data, because of their shallow radial length of investigation.

4.1 Reservoir Description and Location

This field example focuses on data acquired in a tight-gas sandstone reservoir in the Wamsutter field, Wyoming, located in south-central Wyoming within the eastern part of the Greater Green River Basin. Gas production from the Wamsutter is in excess of 500 MMCFD and is derived primarily from the Late Cretaceous, Almond formation. It is divided into upper, middle, and lower Almond components due to variability of petrophysical properties. Porosity is lower than 15% and permeability is lower than 0.1 md. With such low permeabilities, multi-stage hydraulic fracturing is routinely performed in vertical and deviated wells. The Almond formation comprises trangsressive-regressive sediments deposited in fluvial, coastal plain, and shallow marine depositional environments (Tobin et al., 2010).

Almond sandstones are very fine to fine-grained, moderately sorted sublitharenites and litharenites and represent massive, laminated or cross-laminated shoreface and tidal channel facies. Quartz is the dominant mineral that forms the grain framework. Compaction is extensive in the reservoir; presence of quartz and carbonate cements has been reported from mineralogy analysis. Some intragranular porosity is found in the upper Almond component due to grain dissolution. Due to trace amounts of paramagnetic pyrite and pore-lining chlorite in the lower Almond component, NMR measurements are often biased because of strong internal magnetic field gradients caused by these minerals. Presence of such minerals results in much faster decay of magnetization than expected. Chapters 4 and 5 provide details about the data available and their interpretation.

4.2 Two-Dimensional NMR Results

The 2D NMR inversion algorithm discussed in Chapter 2, was applied to NMR field measurements acquired in a gas-bearing depth segment in the upper Almond formation. The data acquired were specifically intended for T_1-T_2 inversion, for which equation (2.5) was slightly modified to read as

$$d(t,TW) = \sum_{j}^{J} \sum_{i}^{I} m_{i,j} (1 - e^{-\frac{TW}{T_{1,j}}}) \cdot e^{-\frac{t}{T_{2,i}}} \,, \tag{4.1}$$

where d represents data, $m_{i,j}$ represents the partial porosity at a certain point on the 2D grid, TW is wait time, T_2 is transverse relaxation, T_1 is longitudinal relaxation, and t is time. Index i designates the discrete range of values for T_2, and j designates the discrete range of values for T_1.

The gas-bearing interval was chosen because of its good petrophysical properties, i.e. relatively high porosity and permeability. Also, rock classification performed with Winland's (r_{35}) method (Pittman, 1992) based on flow units indicated that the depth segment chosen for analysis belonged to the best rock quality in the formation. **Appendix A** discusses the rock classification method and associated results. Several NMR echo decay trains were acquired, each having a specific value of *TW* and *TE*. **Table 4.1** summarizes the acquisition parameters. Echo decay trains acquired with short values of *TW* were aimed at polarizing hydrogen protons within fast decaying fluids only, i.e. clay-bound and capillary-bound water. Long *TW* values were used in some echo trains to polarize the hydrogen protons within all the fluids, especially gas (gas molecules have higher energy than all other formation fluids, thereby requiring longer polarization times). This acquisition strategy made the data set suitable for T_1-T_2 inversion.

Borehole NMR measurements have a sampling rate of 0.5 ft, where an echo-decay sequence consisting of 6 individual spin-echo trains was acquired with the parameters listed in **Table 4.1**. Therefore, for the depth interval of X760-X761 ft, three suites of NMR echo-decay sequences are available. Before performing the 2D inversion, these three echo-decay sequences were stacked to obtain a single, effective echo-decay sequence with 6 echo-decay trains, which was used as the data vector, $\boldsymbol{d}$, in the inversion algorithm to obtain the corresponding 2D NMR map. Stacking was performed by calculating the arithmetic mean of data points acquired at each time sample. Data compression (Section 2.1.1), whenever required, was performed after stacking.

Echo-Decay Number	Number of Echoes (*NE)*	Wait Time (*TW*) [ms]	Inter-Echo Time (*TE*) [ms]
1	10	10	0.6
2	250	6300	1.2
3	125	1500	1.2
4	10	30	0.6
5	10	100	0.6
6	10	300	0.6

Table 4.1: Field Case No. 1 and Field Case No. 2: Parameters used in the acquisition of field NMR data.

Figure 4.1 shows the 2D, T_1-T_2 map estimated for the depth interval X760-X761 ft. A total of 5 fluid signatures are observed on the map; these include gas, water-base mud filtrate, mobile water, capillary-bound water, and clay-bound water. The T_2 distribution includes 4 peaks, which would incorrectly lead one to conclude that there are only 4 pore-saturating fluids, instead of the 5 fluids evidenced by the 2D map. This example confirms that 2D maps have an advantage over conventional 1D NMR interpretations in diagnosing fluid types. The magnitude and lateral spread of each fluid signature on the 2D map determines its relative contribution to total porosity. Careful observation reveals that water-base mud filtrate and mobile water exhibit dominant signatures. Despite the high initial gas saturation for this interval, the NMR gas signature is weak because it is masked by that of invading mud filtrate. This behavior indicates that the formation includes mobile gas and that the depth interval in question could be hydrocarbon-bearing.

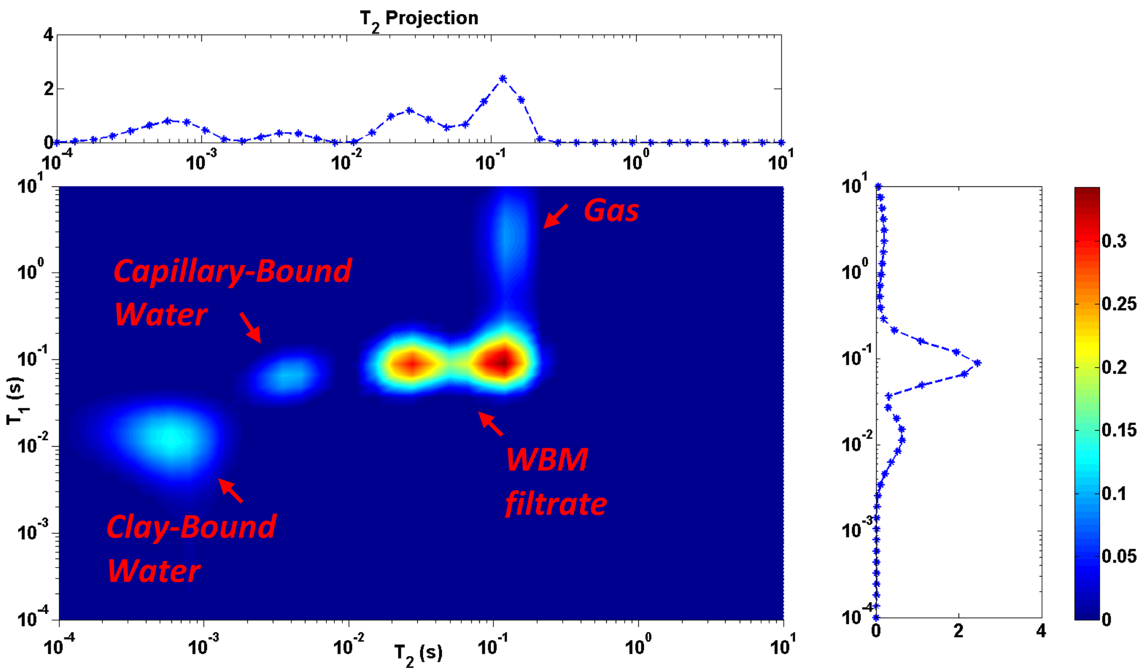

Figure 4.1: Field Case No. 1: T_1-T_2 map calculated for the depth interval X760-X761 ft. Five distinct fluid signatures can be diagnosed from the map. Conventional T_2 and T_1 distributions, shown in the panels on the top and right, respectively, do not have sufficient degrees of freedom to differentiate all the fluid signatures. The color bar to the right describes porosity in percentage.

The estimated T_2 distribution is used to calculate total porosity with the equation

$$\phi_{total,NMR} = \int_{T_{2,low}}^{T_{2.high}} m(T_{2|T_1}) \cdot dT_2 \ , \tag{4.2}$$

where $m(T_2|_{T1})$ designates the value of the function $m(T_2,T_1)$ at a fixed T_1 value. Generally, a long value of T_1 is used for such calculations; $T_{2,low}$ and $T_{2,high}$ are the lower and upper limits for the estimated T_2 distribution, respectively. Equation (4.1) implies that total porosity can be obtained by calculating the area under the T_2 distribution curve. In this example, the calculation yields a total porosity of 14.79% while laboratory measurements performed on core samples report a porosity of 14.88%. The two numbers are in very good agreement. Using a modified version of equation (4.1), the partial porosity for each fluid signature diagnosed on the 2D NMR map is calculated via the equation

$$\phi_{partial,NMR} = \int_{T_{1,low}}^{T_{1,high}} \int_{T_{2,low}}^{T_{2.high}} m(T_2,T_1) \cdot dT_2 \ dT_1 , \tag{4.3}$$

where $m(T_2,T_1)$ designates partial porosity, which is a function of T_1 and T_2 for this data set; $T_{2,low}$ and $T_{2,high}$ are the lower and upper limits, respectively, for the estimated T_2 distribution of a particular fluid, and $T_{1,low}$ and $T_{1,high}$ are the respective limits of the T_1 interval for the selected fluid signature. This calculation enables one to determine the contribution of each diagnosed fluid toward the total pore space. **Table 4.2** reports the partial porosity for fluids calculated from the estimated T_1-T_2 map.

Fluid	Partial Porosity (%)
Gas	1.55
WBM Filtrate	7.31
Capillary-Bound Water	2.37
Clay-Bound Water	3.56

Table 4.2: Field Case No. 1: Partial porosity for fluids calculated from the estimated T_1-T_2 map.

4.3 STATIC AND DYNAMIC MULTI-LAYER MODELS

Figure 4.2 shows the available well logs, together with porosity and water saturation logs calculated via conventional well-log analysis along the depth interval of interest. There is a prominent separation between resistivity logs with different radial lengths of investigation. The gamma-ray log has a relatively low value, indicating low shale concentration. Separation between neutron and density porosity logs (calibrated in limestone porosity units) is also small, indicating low shale concentration and presence of hydrocarbons. Connate water in the upper Almond formation has low salinity, approximately equal to 11,000 ppm of NaCl equivalent. Drilling mud also has low salinity, approximately equal to 7,000 ppm of NaCl equivalent, thereby indicating a relatively low salinity contrast between drilling mud and formation water. Because of the low salinity contrast, it is hypothesized that separation of apparent resistivity logs is chiefly due to the radial invasion front of water. In conventional 1D NMR logs, T_2 and T_1 distributions shift to higher time values than normal, thereby indicating larger pore sizes saturated with light fluids, compared to depth intervals above and below. Also, on the T_1 distribution track, a small signature is observed at very high T_1 values (T_1 > 2 seconds), which indicates presence of gas.

Conventional petrophysical analysis yielded porosity (total and non-shale porosity) and water saturation logs (total and flushed-zone water saturation). The calculated total porosity, ϕ_t, is consistently in good agreement with core measurements except for a small coal-bed interval located around X765 ft (which lies outside the modeling interval). Due to low shale volume in this interval, non-shale porosity, ϕ_{ns}, is very close to ϕ_t. Total water saturation, S_{wt}, was calculated using Archie's equation with deep apparent resistivity (array induction resistivity measurements) and is approximately equal to 40% in this interval. Flushed-zone water saturation, S_{xo}, which was calculated using Archie's equation with shallow apparent resistivity, is approximately 92%. Reservoir temperature in this interval is approximately 180.5 °F. **Table 4.3** reports the Archie's parameters used for the calculation of water saturation.

Archie's Parameters	**Symbol, Units**	**Value**
Tortuosity Factor	a,[]	1
Cementation Exponent	m, []	1.5
Saturation Exponent	n, []	2.05
Connate-Water Resistivity (at 180.5 °F)	R_w, ohm.m	0.25
Mud-Filtrate Resistivity (at 180.5 °F)	R_{mf}, ohm.m	0.33

Table 4.3: Field Case No. 1: Archie's parameters used for the calculation of water saturation.

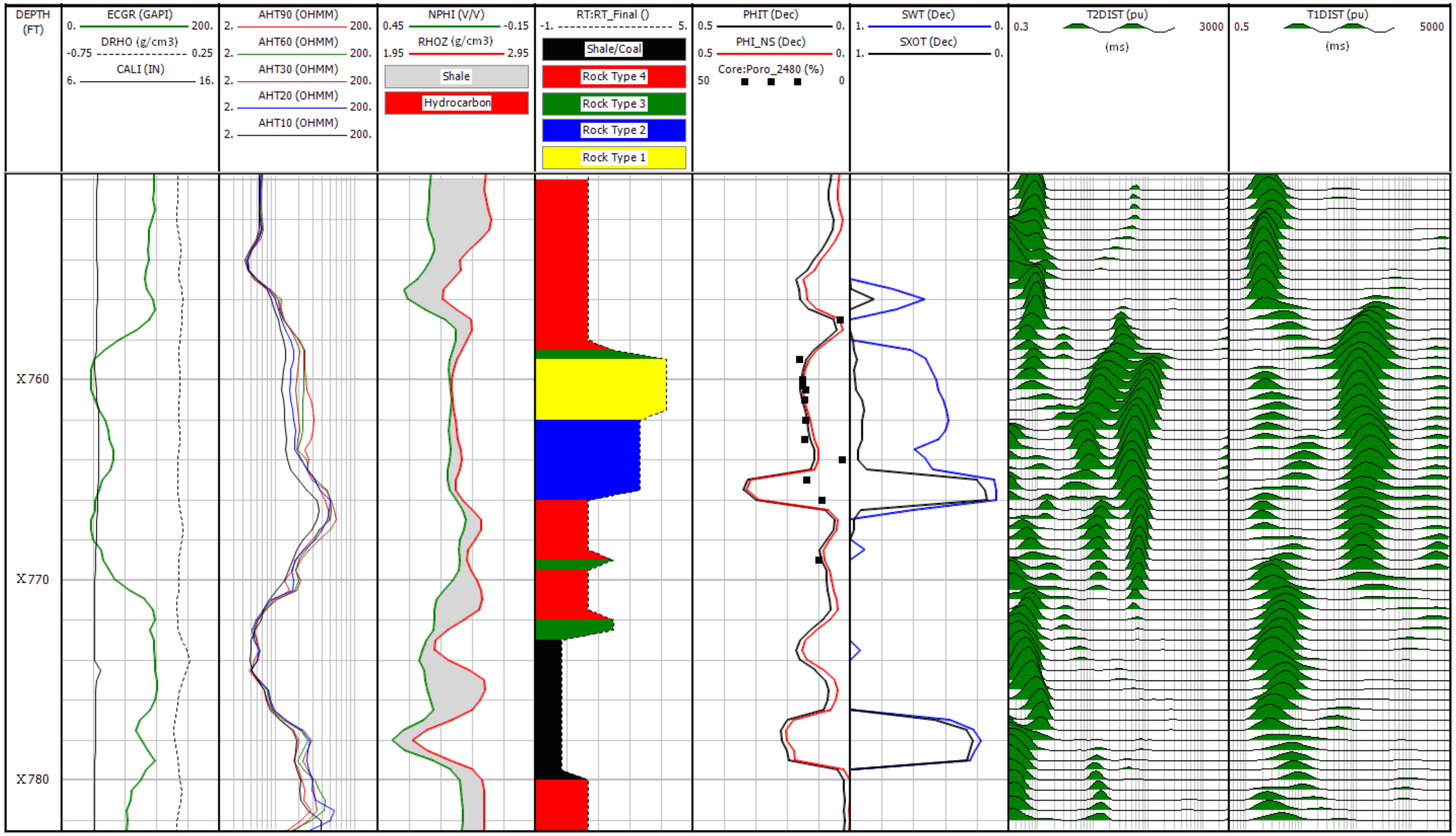

Figure 4.2: Field Case No. 1: Wireline logs along the depth interval of interest. Track 1: depth. Track 2: density correction log, caliper log, and gamma-ray log. Track 3: apparent resistivity logs. Track 4: nuclear logs (neutron porosity is calibrated in limestone porosity units). Track 5: rock types estimated from Winland's method. Track 6: total porosity, non-shale porosity from conventional interpretation, and porosity measurements from core samples. Track 7: total water saturation and flushed-zone water saturation obtained from Archie's equation. Track 8: T_2 distribution. Track 9: T_1 distribution.

Mud-filtrate invasion and fluid displacement are dynamic petrophysical processes. In order to secure reliable values of S_{xo} and movable hydrocarbon saturation, one must perform dynamic simulations of mud-filtrate invasion when constructing multi-layer petrophysical models. Accordingly, in this study the interval of interest was divided into two petrophysical layers, with every layer exhibiting a specific set of static (e.g. porosity, water saturation, mineralogy, shale concentration, and salt concentration) and dynamic petrophysical properties (e.g. permeability, relative permeability, and capillary pressure). These properties were input into the CSF to perform numerical simulations of invasion and corresponding well logs until an acceptable match was obtained between available well logs and their numerical simulations performed with UTAPWeLS[3]. **Figure 4.3** shows the final agreement between well logs and their numerical simulations. **Figure 4.4** shows the radial profile of mud-filtrate invasion simulated after 25 days of invasion. The invasion profile exhibits a smooth radial front and is located approximately 1.5 ft away from the wellbore into the formation. **Table 4.4** summarizes the rock and fluid properties assumed to describe saturation-dependent, water-gas relative permeability and capillary pressure via Brooks-Corey's formulation (Brooks and Corey, 1994). **Figure 4.5** describes the corresponding saturation-dependent, water-gas relative permeability and capillary pressure curves assumed in the simulation of the process of mud-filtrate invasion for this interval. **Table 4.5** describes the mudcake, fluid, and formation properties assumed in the simulation of the process of mud-filtrate invasion. Most of the above mentioned parameters were determined from core analysis and laboratory measurements.

---

[3] Developed by The University of Texas at Austin's Research Consortium on Formation Evaluation.

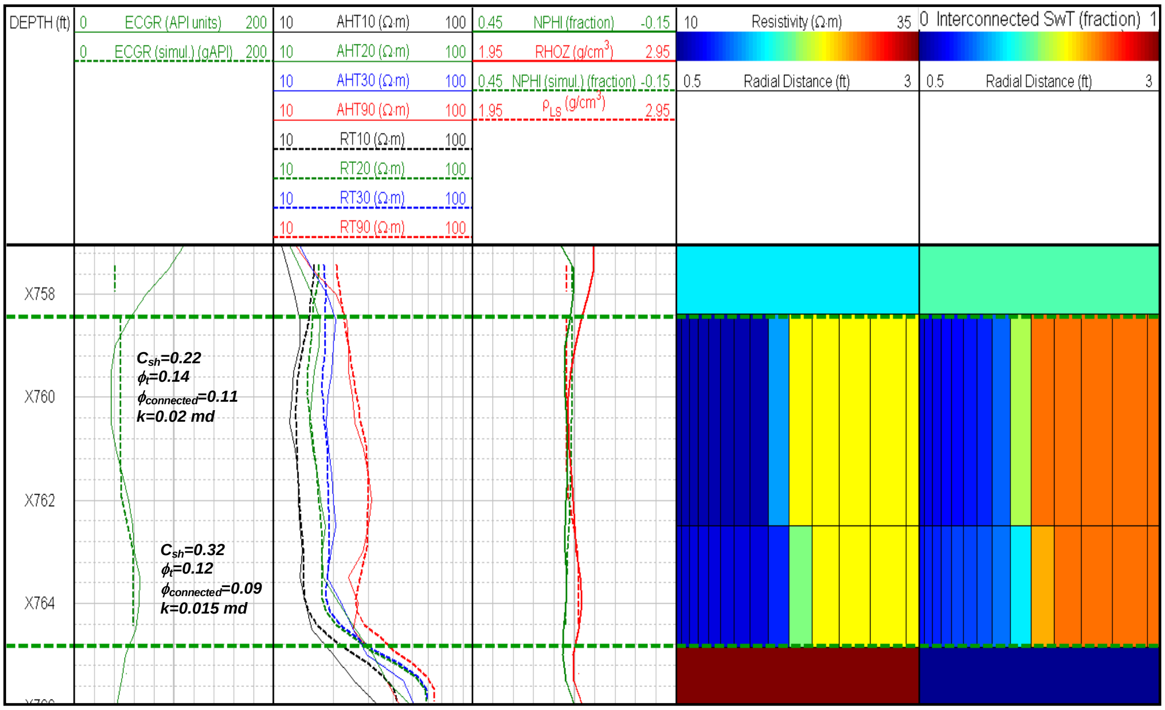

Figure 4.3: Field Case No. 1: Agreement between well logs and their numerical simulation obtained from the CSF. Solid lines identify measured logs while dashed lines identify simulated logs. Track 1: depth. Track 2: gamma-ray log. Track 3: apparent resistivity logs. Track 4: nuclear logs (neutron porosity is calibrated in limestone porosity units). Track 5: radial distribution of resistivity. Track 6: radial distribution of total interconnected water saturation. Only the depth interval included between the two horizontal green lines was considered for numerical simulation.

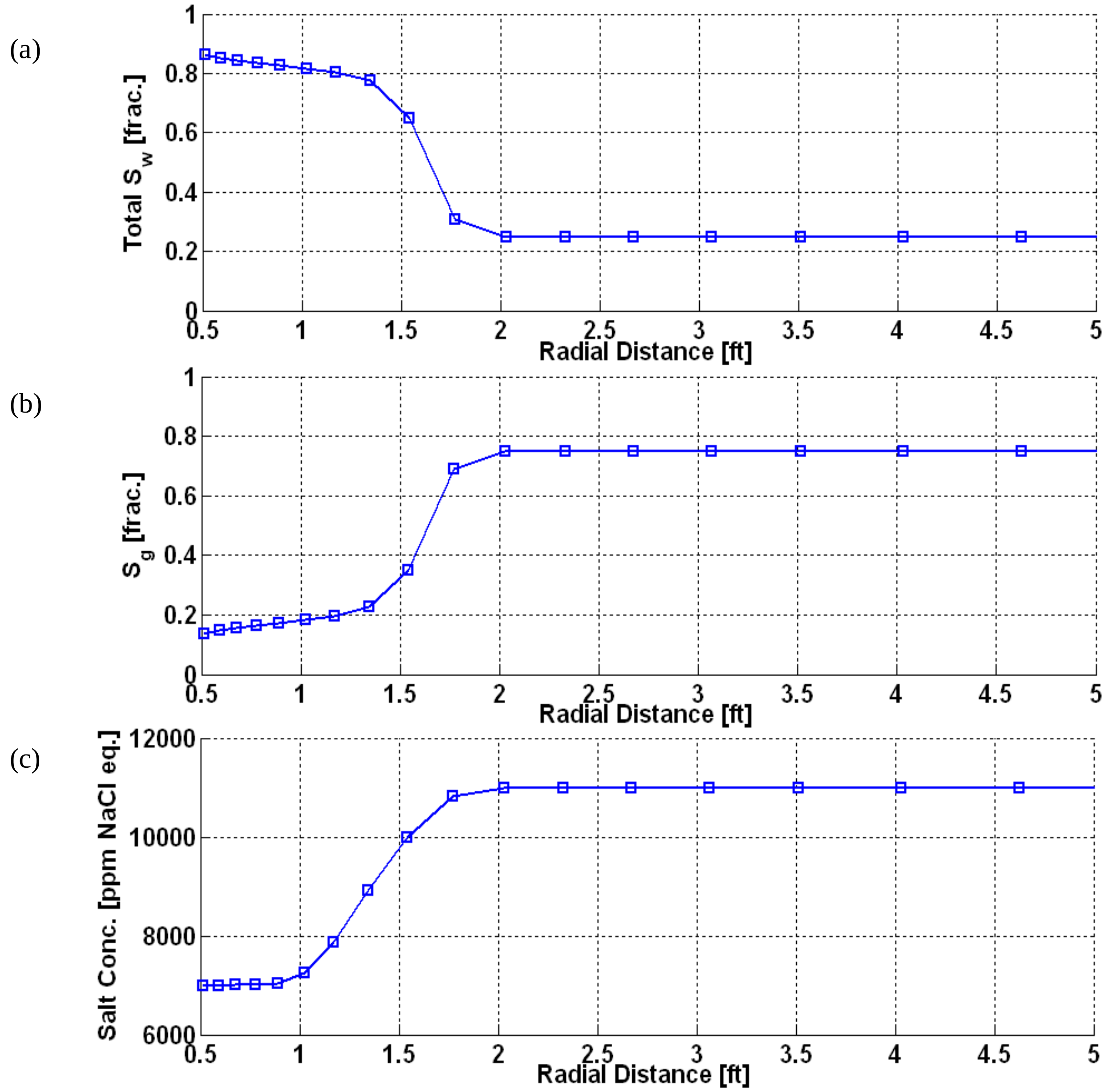

Figure 4.4: Field Case No. 1: Panel (a): Radial profile of total water saturation. Panel (b): Gas saturation. Panel (c): Salt concentration (in NaCl equivalent) calculated with the CSF. The invasion front is radially smooth and is located approximately 1.5 ft into the formation.

S_{gr}	$\phi_{t,ic}$ [%]	k [md]	$P_c^{\,0}$ [psi.D$^{1/2}$]	e_p	k^0_{rnw}	e_{nw}	k^0_{rw}	e_w	S_{wr}
0.05	11	0.02	5	10	0.9	3	0.2	8	0.25
0.1	9	0.015	6	5	0.8	3	0.3	8	0.25

Table 4.4: Field Case No. 1: Rock and fluid properties (Brooks-Corey's parameters) assumed in the simulation of the process of mud-filtrate invasion in the depth interval X760-X761 ft.

While improving the agreement between available well logs and their numerical simulation by adjusting static and dynamic petrophysical properties, it was observed that the best match was secured when non-zero isolated porosity was included in the static properties. Presence of isolated porosity in the upper Almond formation was also confirmed by thin-section petrographic analysis, which indicated presence of grain dissolution. This behavior implies that the CSF must divide total porosity into total porosity, interconnected porosity, and isolated porosity. Simulations of mud-filtrate invasion assume that, due to the water-wet nature of grains, isolated porosity is saturated with connate water. For dynamic simulations as well as for simulations of electrical resistivity, only interconnected porosity governs fluid displacement and salt mixing. Based on these observations and calculations, total porosity was estimated to be 14% out of which 3% was isolated porosity and the remaining 11% was interconnected porosity.

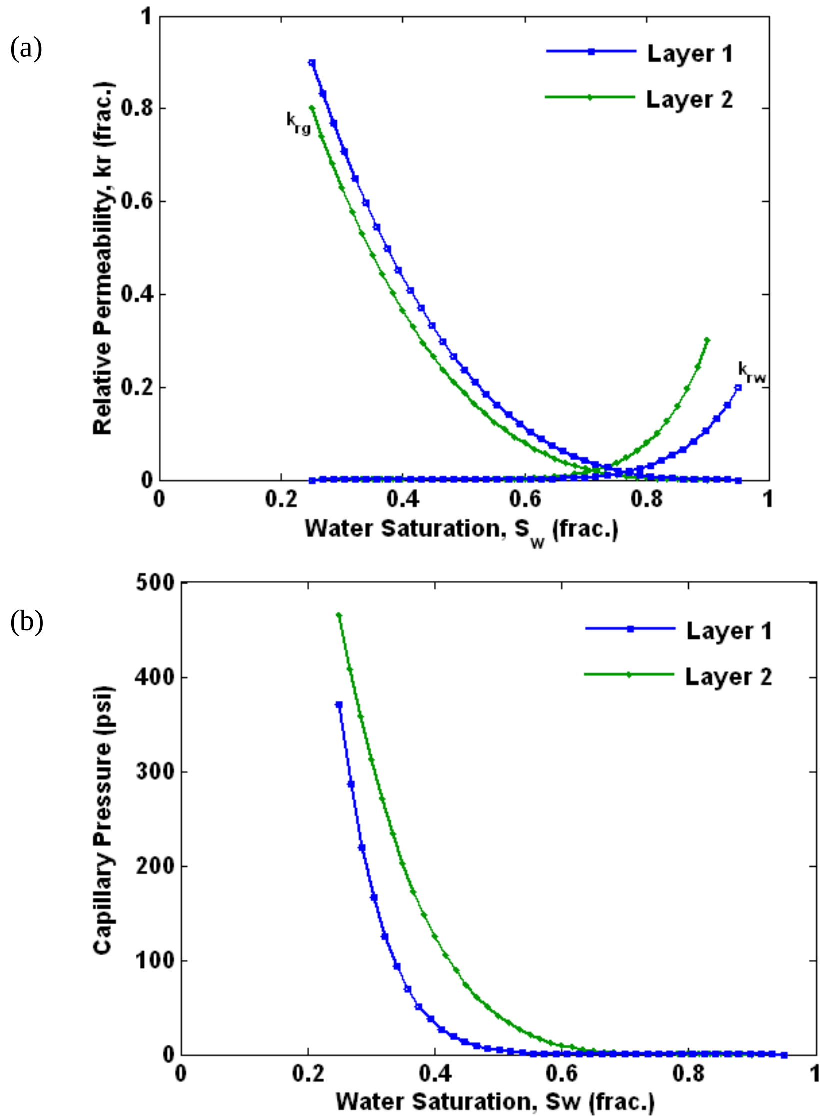

Figure 4.5: Field Case No. 1: Panel (a): Water-gas relative permeability curves. Panel (b): Water-gas capillary pressure curves assumed in the simulation of mud-filtrate invasion for the two petrophysical layers defined within the depth interval of interest.

Variable	Units	Value
Wellbore radius	ft	0.5
Maximum invasion time	days	25
Formation outer boundary	ft	400
Reservoir temperature	ºF	181.5
Initial reservoir pressure	psi	7800
Gas viscosity (reservoir conditions)	cp	0.05
Overbalance pressure	psi	300
Mud-filtrate density (at STP)	g/cm^3	1.00
Mud-filtrate viscosity (at STP)	cp	1.00
Mud-filtrate compressibility (at STP)	psi^{-1}	3.6×10^{-6}
Formation compressibility	psi^{-1}	1×10^{-7}
Mudcake reference permeability	md	0.03
Mudcake reference porosity	frac.	0.2
Mud solid fraction	frac.	0.06
Mudcake maximum thickness	ft	0.033
Mudcake compressibility exponent	frac.	0.40
Mudcake exponent multiplier	frac.	0.10

Table 4.5: Field Case No. 1: Summary of mudcake, fluid, and formation properties assumed in the simulation of the process of mud-filtrate invasion in the depth interval X760-X761 ft.

4.4 Reconciliation of the 2D NMR Map with the CSF

This step appraises and analyzes results obtained with the CSF and the 2D NMR map jointly, in order to estimate and reconcile formation petrophysical properties such as water saturation, and mobile and residual hydrocarbon saturations. The 2D NMR map renders a detailed description of reservoir fluids, but only at a certain radial length of investigation, whereas the CSF provides a radial distribution of fluid saturations. Another benefit of the CSF is its ability to distinguish between total, isolated, and interconnected porosity. Total porosity obtained from the 2D NMR map is within 0.6% error when compared to total porosity measured from core. However, the 2D NMR map can only quantify total porosity and cannot distinguish between isolated and interconnected porosity. This behavior is attributed to the fact that borehole NMR measurements capture magnetization decay of protons within fluids contained in the entire pore space, and within the radial length of investigation of the measurements. Porosity calculations performed from NMR measurements will reflect total porosity, thereby hampering the differentiation between total and isolated porosity.

While constructing the CSF, initial water saturation was assumed to be 25% for this depth interval, which is equal to irreducible water saturation. The remainder of the pore space was assumed to be saturated with gas. Numerical simulation of invasion indicates that water saturation ranges from 92% near the borehole that and it gradually decreases to 25% approximately 1.5 ft into the formation. These calculations suggest that the depth interval under consideration exhibits approximately 8% residual gas saturation and 67% mobile gas saturation.

Using the values indicated in **Table 4.2**, water saturation was calculated from the T_1-T_2 map and compared to results shown in **Figure 4.4** (describing the radial distribution of water saturation estimated from the CSF) to estimate the corresponding radial length of investigation of NMR measurements. For this depth interval, water saturation calculated from the T_1-T_2 map is approximately 85%, which corresponds to the water saturation simulated (water-base mud-filtrate invasion) at approximately 5 in radially into the formation. The analysis therefore indicates that NMR measurements originate from a radial annulus where the pore space is predominantly saturated with water but where gas saturation is still higher than residual gas saturation.

4.5 UNCERTAINTY ANALYSIS

Stability of inversion results is now appraised by adding synthetic Gaussian noise to the already noisy field data. Measurement noise can originate from tool offset and ringing or from borehole washouts. **Figures 4.6** and **4.7** describe the T_1-T_2 uncertainty map and the T_2 uncertainty bars, respectively. Results were obtained by adding 5% normally distributed random noise to the data. As with the synthetic case discussed in Chapter 3, uncertainty is maximum at points where the change of slope is maximum, usually peaks and troughs, and also at low T_2 values, which coincide with the T_2 response of clay-bound and capillary-bound water. Noise present in NMR data translates into uncertainty of petrophysical interpretations. Total porosity and partial porosities for each fluid are calculated directly from the T_2 distribution and the 2D maps, hence noise present in NMR data has a direct impact on those calculations. Applying equation (4.2) to calculate total porosity from borehole NMR measurements yields a value of 14.79%. However, after adding 5% synthetic Gaussian noise, total porosity calculations vary from 13.43% to 17.08% for the 200 noise realizations indicating a maximum variation of approximately 15%.

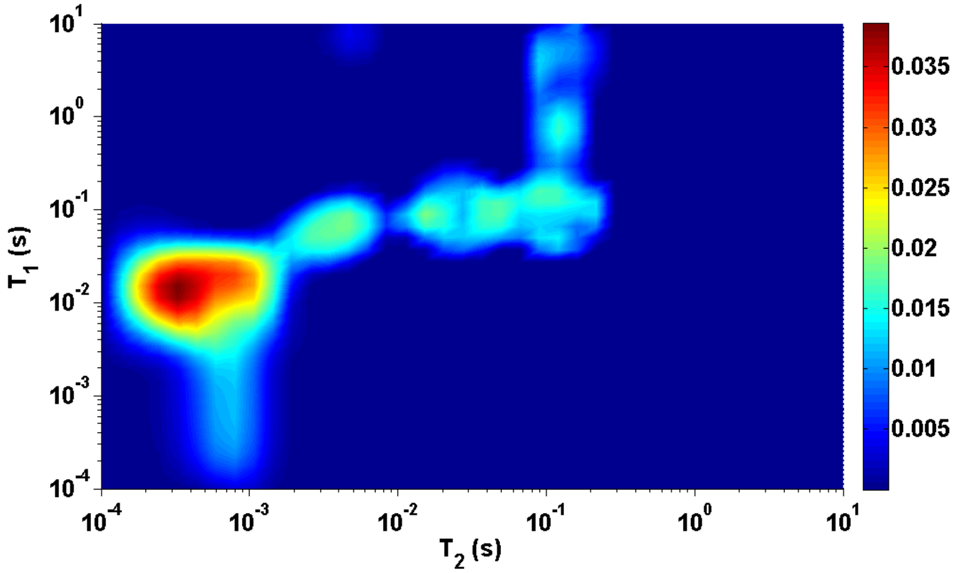

Figure 4.6: Field Case No. 1: T_1-T_2 uncertainty map calculated by adding 5% Gaussian synthetic noise to the field data. Uncertainty is maximum at peaks and troughs of fluid signatures. The color bar to the right describes porosity in percentage.

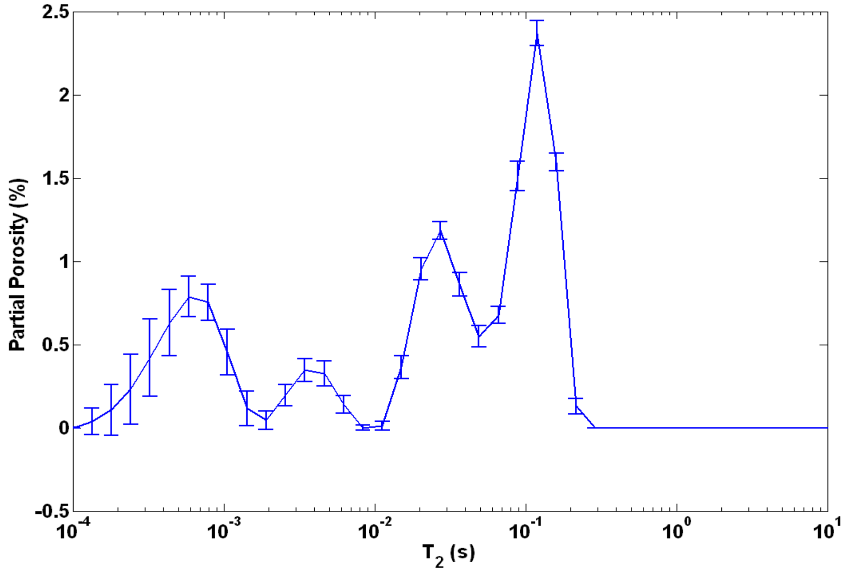

Figure 4.7: Field Case No. 1: Uncertainty bars of the T_2 distribution estimated by adding 5% Gaussian synthetic noise to the data. Uncertainty is maximum at peaks and troughs and at low values of T_2, which correspond to clay-bound and capillary-bound water signatures.

Chapter 5: Field Case No. 2: Tight-Gas Siliciclastic Formation

The second field example considers the same reservoir discussed in Field Case No. 1, but at a different depth interval, located within the lower Almond formation. This field case is intended to appraise the reliability of the 2D NMR inversion algorithm and to verify its consistency with multi-layer static and dynamic petrophysical models constructed with the CSF. It has been found that compaction effects on the lower Almond formation are smaller than those on the upper Almond formation but that it exhibits significantly more cementation, together with presence of pyrite and chlorite. These minerals generate abnormal internal magnetic fields, thereby hindering the interpretation of NMR data.

5.1 Two-Dimensional NMR Results

Figure 5.1 shows the T_1-T_2 map estimated for the depth interval XX08-XX10 ft. Sampling rate of the NMR tool was 0.5 ft and stacking of borehole NMR measurements was performed for this interval, similar to that explained in Section 4.2. Rock classification performed with Winland's (r_{35}) method (Pittman, 1992) based on flow units indicates that this depth interval includes the second best petrophysical rock quality in the formation, out of the five rock types diagnosed from rock typing. **Appendix A** discusses the rock classification method and associated results. Echo-decay trains were acquired with the same properties described in **Table 4.1**. We observe four fluid signatures on the 2D NMR map for this depth interval, which include gas, water-base mud filtrate, and mobile water. The fourth signature, whose peak can be observed at a high T_1 value and a low T_2 value, is ambiguous and therefore merits further investigation for reliable appraisal. Mineralogy analysis indicates that this depth interval includes some pyrite and pore-lining chlorite. Both these minerals give rise to relatively strong internal magnetic field gradients due to large magnetic susceptibility contrast with surrounding pore fluids. Rock internal magnetic field gradients result in echo-spacing shortening of the NMR T_2 relaxation time distribution and large T_1/T_2 ratios (Shafer et al., 2004). Presence of minerals with strong internal magnetic field gradients decreases the ability of NMR tools to polarize the hydrogen protons within saturating fluids. This behavior leads to an abnormally large polarization time response, T_1, and an extremely fast magnetization decay, corresponding to a smaller than expected value of T_2. Consequently, the T_1/T_2 ratio is abnormally large, making fluid typing challenging.

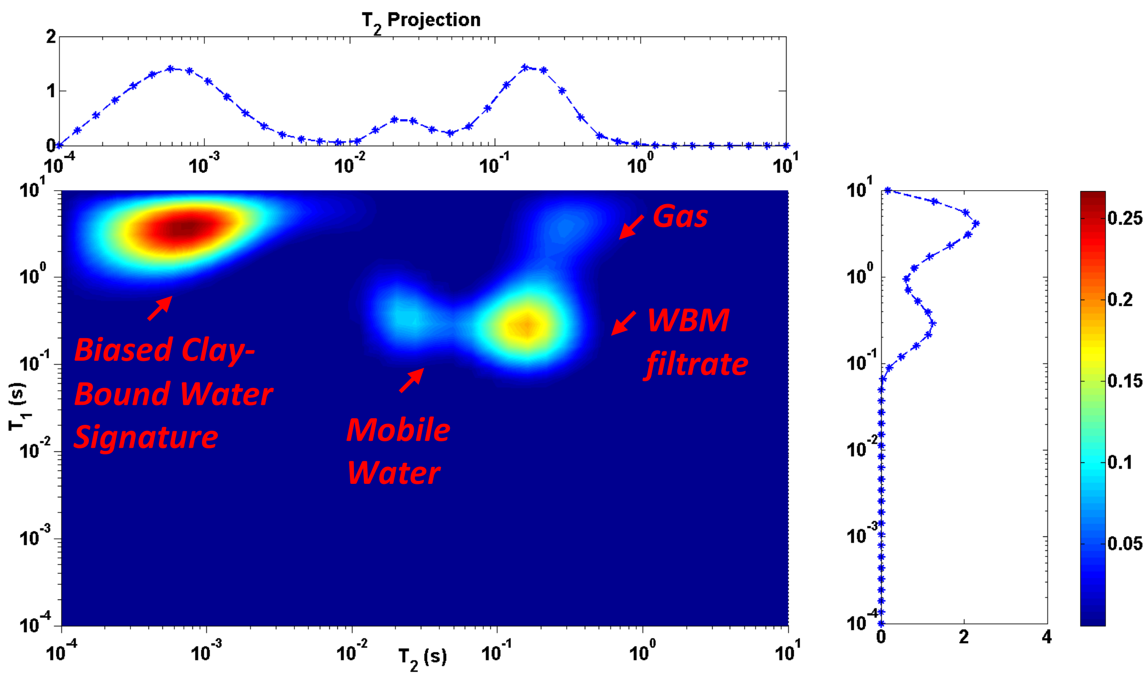

Figure 5.1: Field Case No. 2: T_1-T_2 map obtained for the depth interval XX08-XX10 ft. Four distinct fluid signatures can be diagnosed from the map. Conventional T_2 and T_1 distributions, shown in the panels on the top and right, respectively, do not have sufficient degrees of freedom to differentiate all the fluid signatures. An anomalous fluid signature (on the top left of the map) with high T_1/T_2 value is diagnosed because of the presence of minerals with strong internal magnetic field gradients. The color bar to the right describes porosity in percentage.

The relative magnitude and spread of each fluid signature on the 2D NMR map suggests the corresponding contribution to total porosity. Excluding the anomalous peak, the most dominant peak in this case corresponds to that of water-base mud filtrate, followed by the peaks of mobile water and gas. It is evident from the 2D NMR map that the radial length of investigation of NMR measurements is within the radial zone which has been invaded by mud filtrate. Total porosity calculated from the NMR T_2 distribution is 17.35% while laboratory measurements of total porosity report 11.26%. This discrepancy is due to presence of internal field gradients. **Table 5.1** reports the partial porosity of each fluid signature calculated with the 2D NMR map.

Fluid	Partial Porosity (%)
Gas	1.31
WBM Filtrate	5.37
Mobile Water	1.64
Clay-Bound Water	9.03

Table 5.1: Field Case No. 2: Partial porosity for fluids calculated from the estimated T_1-T_2 map.

Two-dimensional NMR results are not reliable here because of the presence of minerals which cause internal field gradients but they do convey important information regarding saturating fluids and partial porosity. **Figure 5.1** indicates that conventional 1D NMR interpretation results, shown in the T_2 projection panel, cannot differentiate between the fluid signatures of gas and mud filtrate. This behavior is due to the fact that T_{2B} values for gas and mud filtrate lie in the same numerical range. Likewise, calculation of partial porosity for the identified fluids is challenging in the case of 1D interpretation because of overlapping T_2 spectra, especially for gas and mud filtrate. The contrast in T_1 values, however, makes fluid identification more reliable when performed from the T_1-T_2 map.

5.2 Static and Dynamic Multi-Layer Models

For the depth interval of interest, **Figure 5.2** shows the available field logs including gamma ray, apparent resistivity, density, neutron, and T_2 and T_1 spectra, combined with porosity and water saturations logs calculated via conventional analysis. Apparent resistivity logs with different radial lengths of investigation exhibit separation but it is not as significant as in Field Case No. 1. The gamma-ray log has relatively low values, indicating low shale concentration. Nuclear and density porosity logs (calibrated in limestone porosity units) exhibit a distinct cross-over and 1D T_1 logs exhibit a shift toward higher time values. Both these characteristics observed in the available logs indicate presence of gas. Salinity contrast between connate water (approximately equal to 11,000 ppm NaCl equivalent) and drilling mud (approximately equal to 8,500 ppm NaCl equivalent) is low, suggesting that the separation between apparent resistivity logs can be attributed to radial variations of water saturation resulting from water-base mud-filtrate invasion.

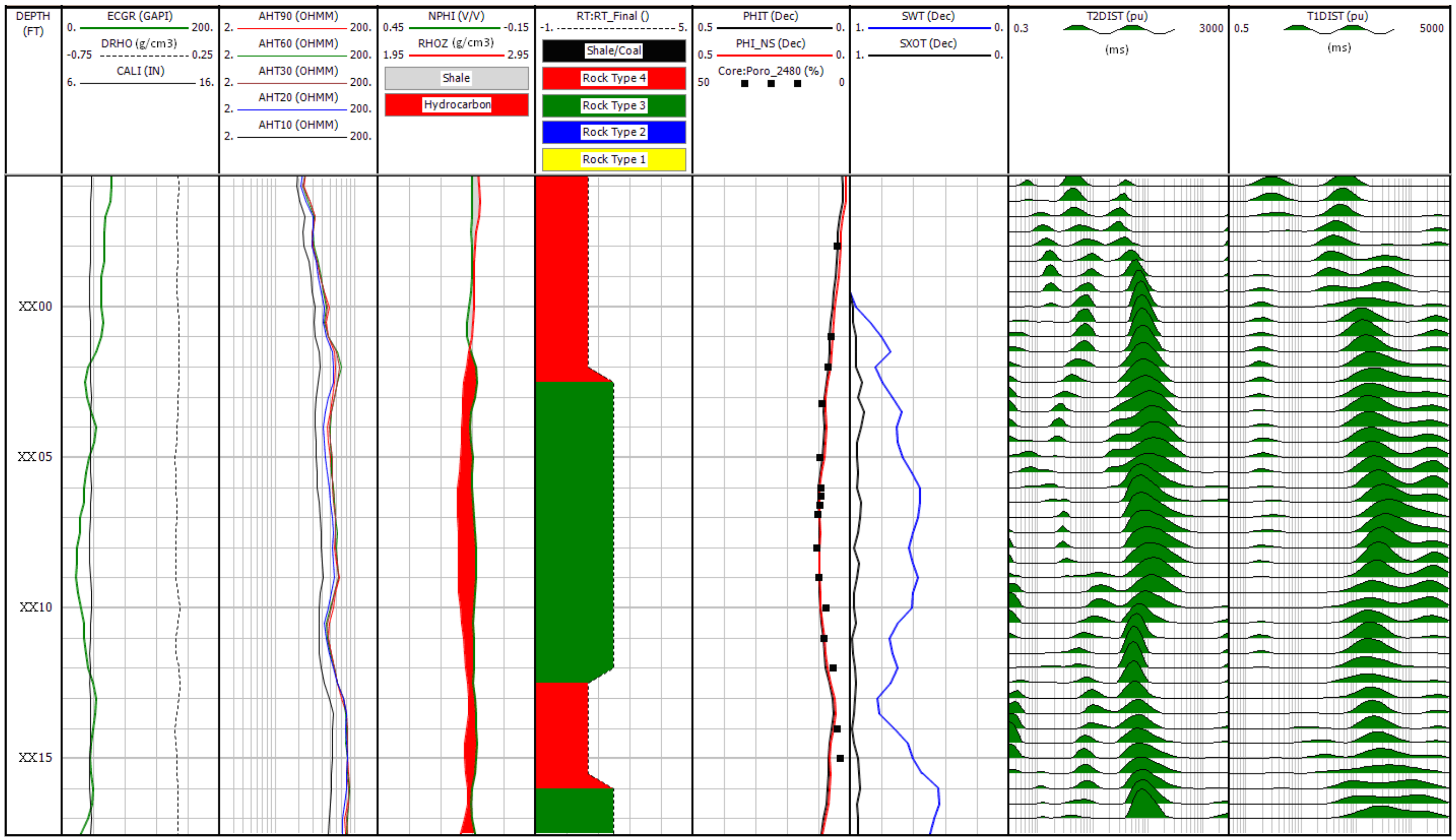

Figure 5.2: Field Case No. 2: Wireline logs along the depth interval of interest. Track 1: depth. Track 2: density correction log, caliper log, and gamma-ray log. Track 3: apparent resistivity logs. Track 4: nuclear logs (neutron porosity is calibrated in limestone porosity units). Track 5: rock types estimated from Winland's method. Track 6: total porosity, non-shale porosity from conventional interpretation, and porosity measurements from core samples. Track 7: total water saturation and flushed-zone water saturation obtained from Archie's equation. Track 8: T_2 distribution. Track 9: T_1 distribution.

Total porosity (ϕ_t) calculated with conventional petrophysical analysis is in good agreement with core measurements. Volumetric concentration of shale for this depth interval was calculated jointly from nuclear and gamma-ray logs to be approximately 20%. Total water saturation, S_{wt}, calculated with Archie's equation and deep apparent resistivity (array induction measurement), is approximately 60% in this interval while flushed-zone water saturation, S_{xo}, calculated with Archie's equation and shallow apparent resistivity, is approximately 93%. Reservoir temperature for this interval is approximately 186.9 °F. **Table 5.2** reports Archie's parameters used for the calculation of water saturation.

Archie's Parameters	**Symbol, Units**	**Value**
Tortuosity Factor	a,[]	1
Cementation Exponent	m, []	1.5
Saturation Exponent	n, []	2.05
Connate-Water Resistivity (at 186.9 °F)	R_w, ohm.m	0.22
Mud-Filtrate Resistivity (at 186.9 °F)	R_{mf}, ohm.m	0.28

Table 5.2: Field Case No. 2: Archie's parameters used for the calculation of water saturation.

To estimate radial distribution of water and hydrocarbon in the formation, the corresponding CSF is constructed to numerically simulate the process of mud-filtrate invasion. The depth interval of interest was divided into two petrophysical layers and the CSF was constructed using UTAPWeLS[4]. **Figure 5.3** shows the final match between available well logs and their numerical simulations. **Figure 5.4** shows the radial distribution of water saturation resulting from 25 days of invasion. The invasion front exhibits a sharp slope and is located at a radial distance of approximately 0.6 ft into the formation.

[4] Developed by The University of Texas at Austin's Research Consortium on Formation Evaluation.

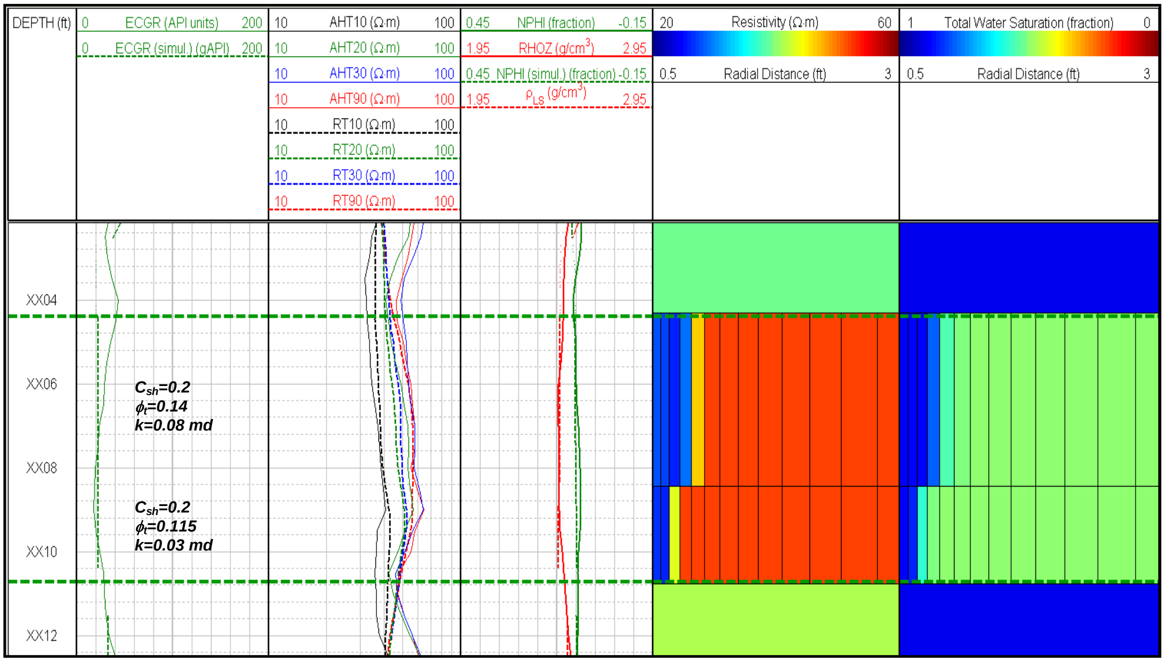

Figure 5.3: Field Case No. 2: Agreement between well logs and their numerical simulation obtained with the CSF. Solid lines identify the measured logs while dashed lines identify simulated logs. Track 1: depth. Track 2: gamma-ray log. Track 3: apparent resistivity logs. Track 4: nuclear logs (neutron porosity is calibrated in limestone porosity units). Track 5: radial distribution of resistivity. Track 6: radial distribution of total interconnected water saturation. Only the depth interval included between the two horizontal green lines was considered for numerical simulation.

(a)

(b)

(c)

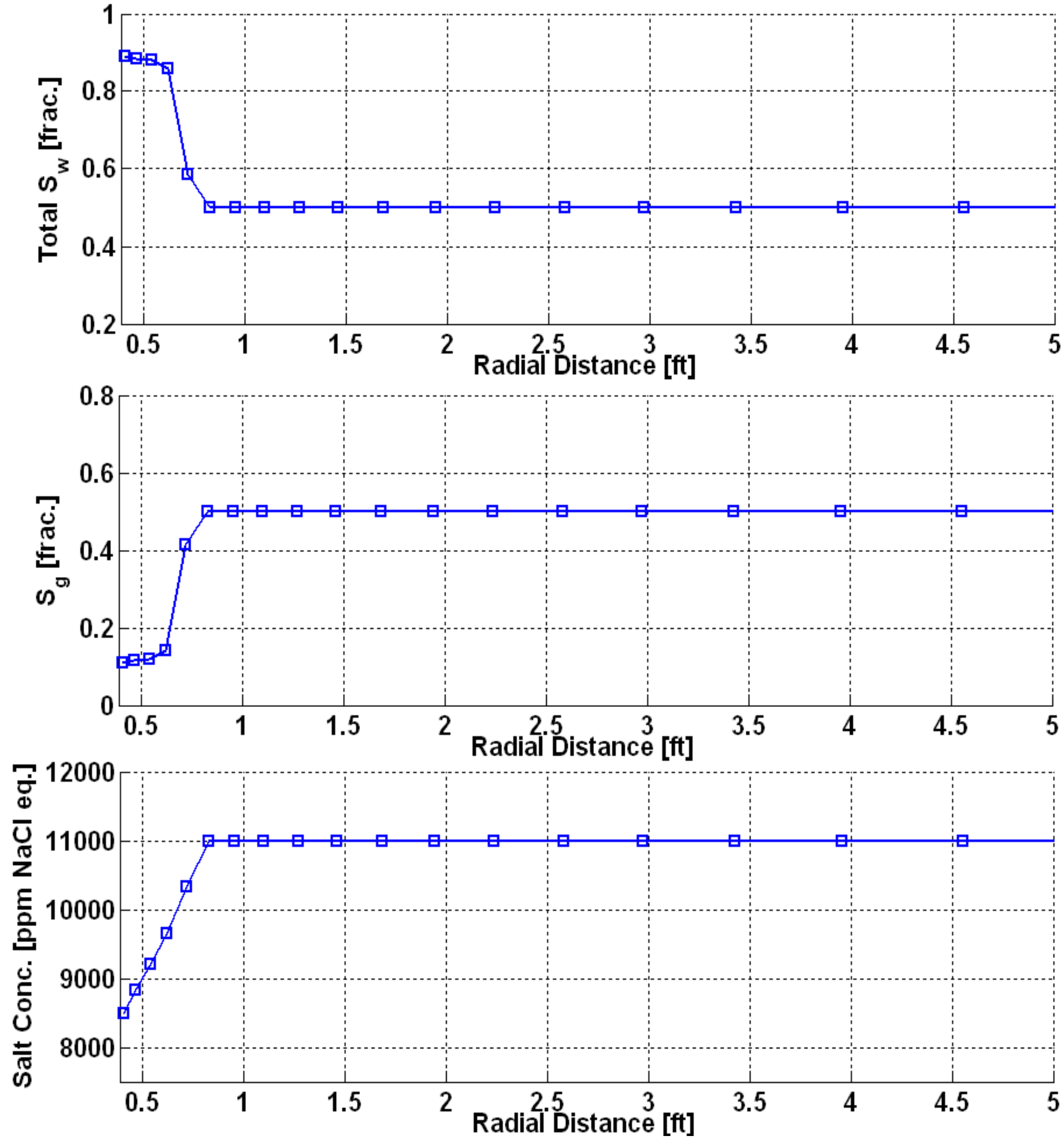

Figure 5.4: Field Case No. 2: Panel (a): Radial profile of total water saturation. Panel (b): Gas saturation. Panel (c): Salt concentration (in NaCl equivalent) calculated with the CSF. The invasion front is steep and is located approximately 0.6 ft into the formation.

Table 5.3 summarizes the rock and fluid properties assumed in the description of saturation-dependent, water-gas relative permeability and capillary pressure via Brooks-

Corey's formulation (Brooks and Corey, 1994). **Figure 5.5** describes the corresponding saturation-dependent, water-gas relative permeability and capillary pressure assumed to simulate the process of mud-filtrate invasion. **Table 5.4** describes the mudcake, fluid, and formation properties assumed in the simulation of the process of mud-filtrate invasion.

S_{gr}	ϕ_t [%]	k [md]	P_c^0 [psi.D$^{1/2}$]	e_p	k^0_{rnw}	e_{nw}	k^0_{rw}	e_w	S_{wr}
0.1	12	0.08	5	10	0.9	2.5	0.2	8	0.3
0.1	11.5	0.03	6	15	0.8	2.5	0.25	8	0.3

Table 5.3: Field Case No. 2: Rock and fluid properties (Brooks-Corey's parameters) assumed in the simulation of the process of mud-filtrate invasion in the depth interval XX08-XX10 ft.

(a)

(b)

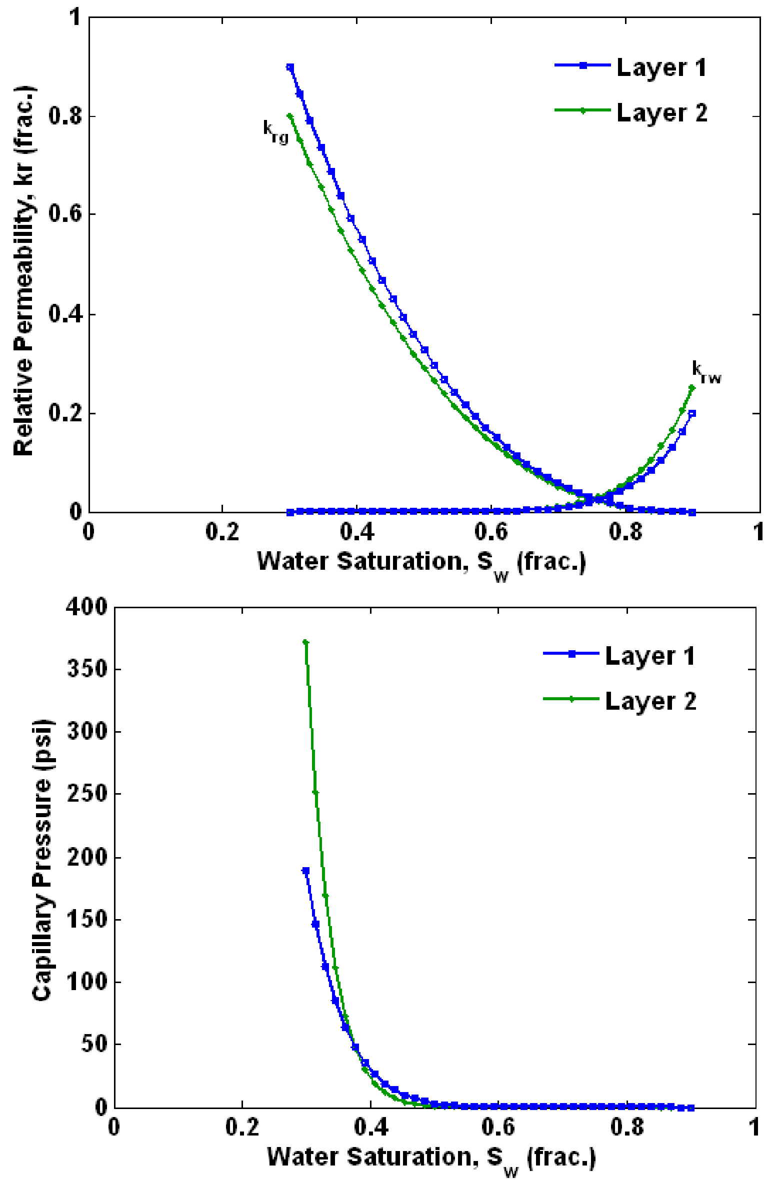

Figure 5.5: Field Case No. 2: Panel (a): Water-gas relative permeability curves. Panel (b) Water-gas capillary pressure curves assumed in the simulation of mud-filtrate invasion for the two petrophysical layers defined within the depth interval of interest.

Variable	Units	Value
Wellbore radius	ft	0.375
Maximum invasion time	days	25
Formation outer boundary	ft	400
Reservoir temperature	ºF	187
Initial reservoir pressure	psi	9500
Gas viscosity (reservoir conditions)	cp	0.05
Overbalance pressure	psi	100
Mud-filtrate density (at STP)	g/cm^3	1.00
Mud-filtrate viscosity (at STP)	cp	1.00
Mud-filtrate compressibility (at STP)	psi^{-1}	3.6×10^{-6}
Formation compressibility	psi^{-1}	1×10^{-7}
Mudcake reference permeability	md	0.03
Mudcake reference porosity	frac.	0.30
Mud solid fraction	frac.	0.06
Mudcake maximum thickness	ft	0.033
Mudcake compressibility exponent	frac.	0.40
Mudcake exponent multiplier	frac.	0.10

Table 5.4: Field Case No. 2: Summary of mudcake, fluid, and formation properties assumed in the simulation of the process of mud-filtrate invasion for the depth interval XX08-XX10 ft.

5.3 Reconciliation of the 2D NMR Map with the CSF

This section describes the joint appraisal of results estimated from the 2D NMR map and the CSF, discussed in Sections 5.1 and 5.2, respectively, with the objective of securing reliable estimations of formation petrophysical properties such as mobile and residual hydrocarbon saturation. As mentioned in Section 5.1, total porosity estimated from NMR measurements was 17.35%. This calculation is approximately 6% higher than the total porosity of 11.26% reported by core analysis. Such an inaccurate calculation originates from the presence of pyrite and chlorite in the studied depth interval. As explained in Section 5.1, these minerals adversely affect NMR measurements because of their strong internal magnetic field gradients. The alternative to accurately estimate total porosity was to construct the CSF. Multi-layer static and dynamic petrophysical simulations performed with the CSF for this depth interval yielded a total porosity of 11.50%, which is found to be in good agreement with total porosity of 11.26% reported by core analysis.

As shown in **Figure 5.2**, rock typing performed on this depth interval indicated that it exhibits medium-quality rocks, suggesting the presence of small pore-throats and therefore, high irreducible water saturation. While constructing the CSF, initial water saturation was assumed to be 50%, out of which 30% was irreducible water saturation. The former assumption also implies that the remainder 50% of the pore space was saturated with gas. **Figure 5.4** shows the radial distribution of water saturation obtained from the simulation of mud-filtrate invasion. Water saturation was estimated to range from 88% near the borehole to approximately 50%, at 0.6 ft radially into the formation. These estimates indicate that under uninvaded reservoir conditions, the depth interval being studied exhibits approximately 12% residual gas saturation, 38% mobile gas saturation, and total water saturation of 50%.

Water saturation calculated from the partial porosity of fluids (excluding the biased clay-bound water signature) reported in **Table 5.1** is 82%. When compared to the radial distribution of water saturation obtained from the CSF, shown in **Figure 5.4**, it is found that the approximate radial length of investigation of NMR measurements is about 5 in. Similar to the observation in Field Case No. 1, these calculations suggest that the NMR tool acquired signals from a radial distance where the pore space was predominantly saturated with water but where gas saturation was slightly higher than residual gas saturation.

5.4 UNCERTAINTY ANALYSIS

This section evaluates the robustness of 2D NMR inversion by adding synthetically generated, 5% Gaussian noise to the acquired field data. **Figures 5.6** and **5.7** show the resulting T_1-T_2 uncertainty map and T_2 uncertainty bars, respectively. It is found that uncertainty is maximum at the location of the biased clay-bound water signature. Such a behavior is due to the fact that hydrogen protons in the fluids are not fully polarized by the NMR tool in the presence of minerals with strong internal magnetic field gradients, resulting in abnormally low T_2 values and high uncertainty. Equations (4.2) and (4.3) show that uncertainty in the T_2 distribution and the 2D NMR map directly affects the estimations of total and partial porosity. Adding 5% synthetic Gaussian noise to the borehole NMR measurements for 200 noise realizations resulted in a maximum error in porosity calculation of approximately 9.75%.

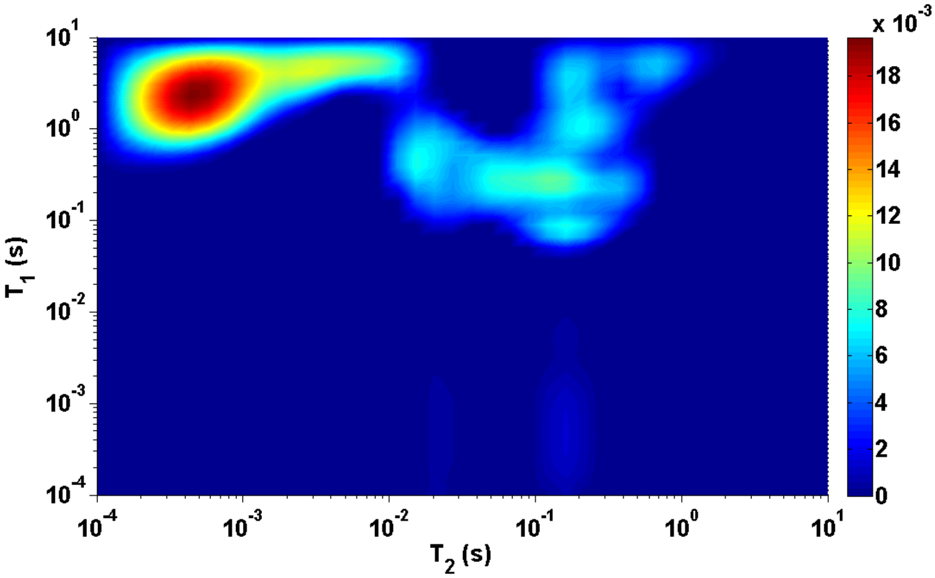

Figure 5.6: Field Case No. 2: T_1-T_2 uncertainty map calculated by adding 5% Gaussian synthetic noise to the field data. Uncertainty is maximum at peaks and troughs of fluid signatures. The color bar to the right describes porosity in percentage.

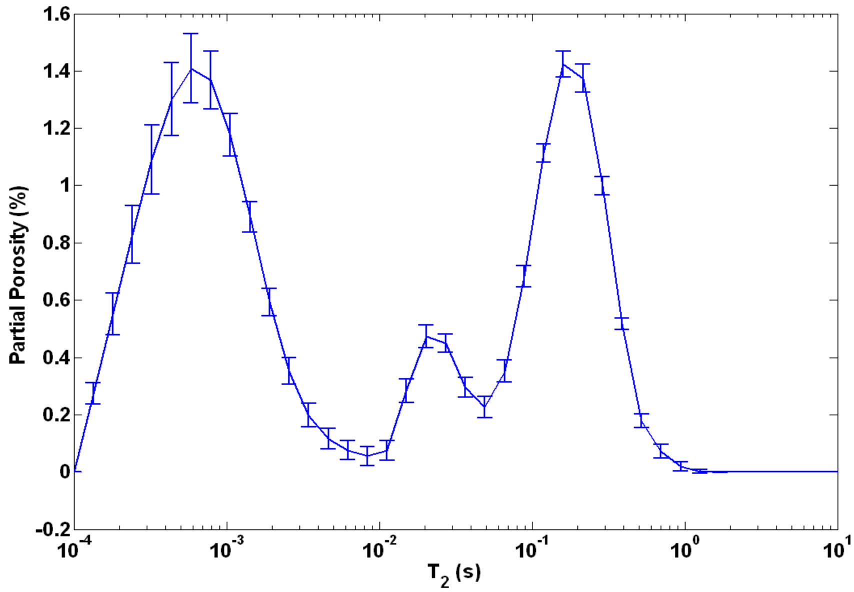

Figure 5.7: Field Case No. 2: Uncertainty bars for the T_2 distribution estimated by adding 5% Gaussian synthetic noise to the data. Uncertainty is maximum at peaks and troughs and at low values of T_2, which correspond to clay-bound and capillary-bound water signatures.

Chapter 6: Field Case No. 3: Siliciclastic Gas Formation

The third field case highlights the importance of reconciling 2D NMR measurements with interpretations made from available well logs. Limited data in the form of Logging-While-Drilling (LWD) apparent resistivity and nuclear logs were available for this case which restricted the construction of the CSF to a multi-layer static model only. This chapter describes results and conclusions stemming from the combined analysis of NMR measurements and available LWD measurements.

6.1 Reservoir Description and Location

The field case focuses on data acquired in a sandstone reservoir in the Fiume Treste Stoccaggio field located in the Abruzzo region of Italy. It is a Pleistocene formation with porosity lower than 25%. An interesting feature about this field is that, over geologic time, hydrocarbons have been displaced by an active underlying aquifer. The pressure trap holding in-situ fluids was breached, resulting in water from the aquifer sweeping the hydrocarbon-bearing zone and leaving only residual gas in the pore space.

6.2 Two-Dimensional NMR Results

For this field example, 2D NMR data were inverted to estimate a T_2-D map, unlike Field Cases No. 1 and 2 where the estimation yielded T_1-T_2 maps. To obtain borehole NMR data suitable for T_2-D inversion, a range of frequencies were used for the acquisition process in order to polarize different radial zones in the formation. At each sampling depth, 24 unique CPMG echo-decay trains were acquired with a sampling rate of 0.5 ft. **Table 6.1** lists the parameters used for acquisition of CPMG echo-decay sequences.

Echo-Decay Number	Frequency [kHz]	Number of Echoes (*NE*)	Wait Time (*TW*) [ms]	Inter-Echo Time (*TE*) [ms]
1	768	1000	9300	0.4
2	768	33	20	0.3
3	962	148	8400	2.7
4	962	33	20	0.3
5	768	1000	1009	0.4
6	768	33	20	0.3
7	962	148	1011	2.7
8	962	33	20	0.3
9	962	25	50	0.4
10	962	25	100	0.4
11	688	148	9300	2.7
12	688	33	20	0.3
13	859	285	8400	1.4
14	859	33	20	0.3
15	688	148	1032	2.7
16	688	33	20	0.3

Table 6.1 (continued)

17	859	285	1037	1.4
18	859	33	20	0.3
19	859	25	50	0.4
20	859	25	100	0.4
21	613	1000	11000	0.4
22	613	33	20	0.3
23	555	1000	11000	0.4
24	555	33	20	0.3

Table 6.1: Field Case No. 3: Parameters used in the acquisition of field NMR data.

Figure 6.1 shows the T_2-D map estimated for the depth interval X39-X41 ft. Stacking of borehole NMR measurements was performed for this interval, following the same procedure explained in Section 4.2. Three important fluid signatures are diagnosed on the map: gas, mobile water, and capillary-bound water. Calculations performed on borehole NMR measurements yielded a total porosity of 17.92%. **Table 6.2** reports partial porosities of fluids estimated from the T_2-D map. From the signatures diagnosed on the T_2-D map and partial porosity calculations, mobile water is determined to be the dominant fluid in the depth interval of interest. This conclusion is also supported by the geologic history of the field and production data alluded to earlier.

The two water components identified on the T_2-D map, i.e. mobile water and capillary-bound water, exhibit elongated signatures along the fluid diffusivity axis, indicating a long range of diffusivity values. This abnormal behavior could be attributed to the phenomenon of restricted diffusion which is found to be significant when a fluid is confined in small pores because molecular diffusion is partially restricted by the size of the pores (Coates et al., 1993). However, restricted diffusion is not expected in this depth interval because of its high porosity of 17.92%. The other hypothesis for this behavior could be that the measurements did not include sufficient magnetic gradients, *G*, to accurately capture the diffusion of hydrogen protons in mobile water.

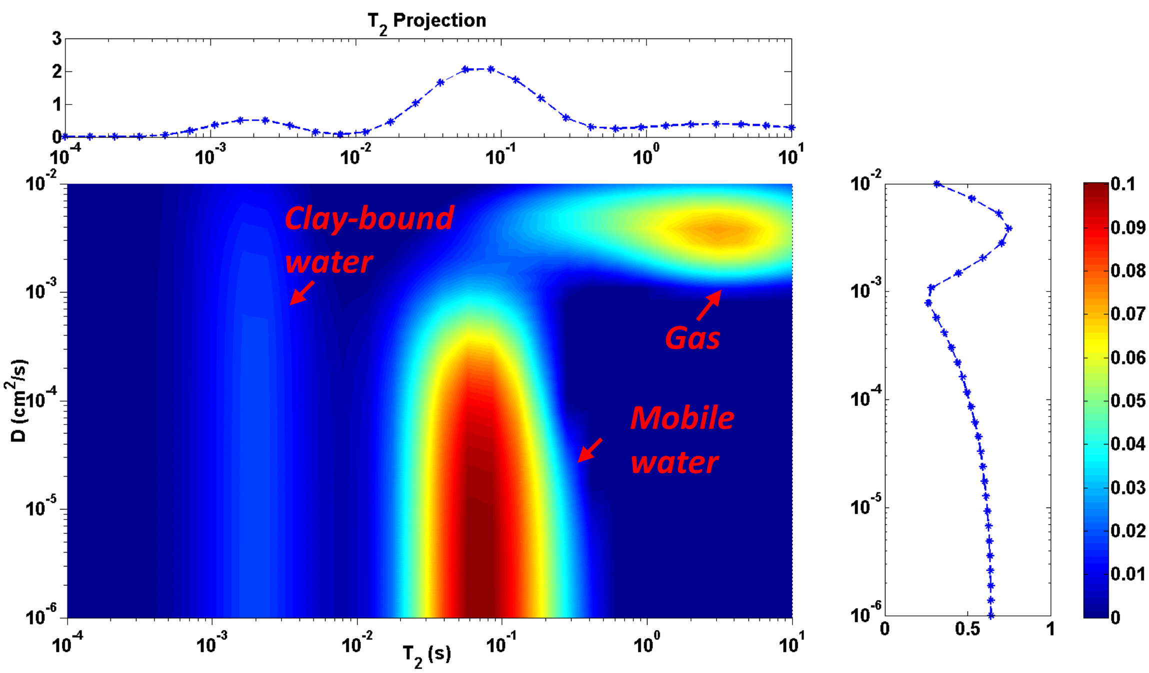

Figure 6.1: Field Case No. 3: T_2-D map obtained for the depth interval X39-X41 ft. Three distinct fluid signatures can be identified from the map. The color bar to the right describes porosity in percentage.

Fluid	Partial Porosity (%)
Gas	3.41
Mobile Water	11.65
Clay-Bound Water	2.86

Table 6.2: Field Case No. 3: Partial porosity for the three fluids identified from the estimated T_2-D map.

6.3 Static Multi-Layer Models and Reconciliation with NMR Data

Available measurements include LWD apparent resistivity and nuclear logs. From **Figure 6.2**, it is observed that apparent resistivity logs with different radial lengths of investigation stack (i.e., they exhibit null separation). A probable reason for this behavior is the fact that because the formation was logged while drilling, the invading water-base mud-filtrate did not penetrate a significant radial distance into the formation. **Figure 6.2** also describes results obtained from conventional interpretations for total and non-shale porosity, total water saturation and volumetric concentration of shale; S_w was calculated using Archie's equation. **Table 6.3** reports the values for a, m, and n for Archie's equation obtained from core data. Formation temperature in this interval is 120.2 °F and connate-water salinity, C_w, is 34,000 ppm of NaCl equivalent. Conventional petrophysical analysis yielded average values of total porosity and water saturation approximately equal to 18.5% and 75%, respectively.

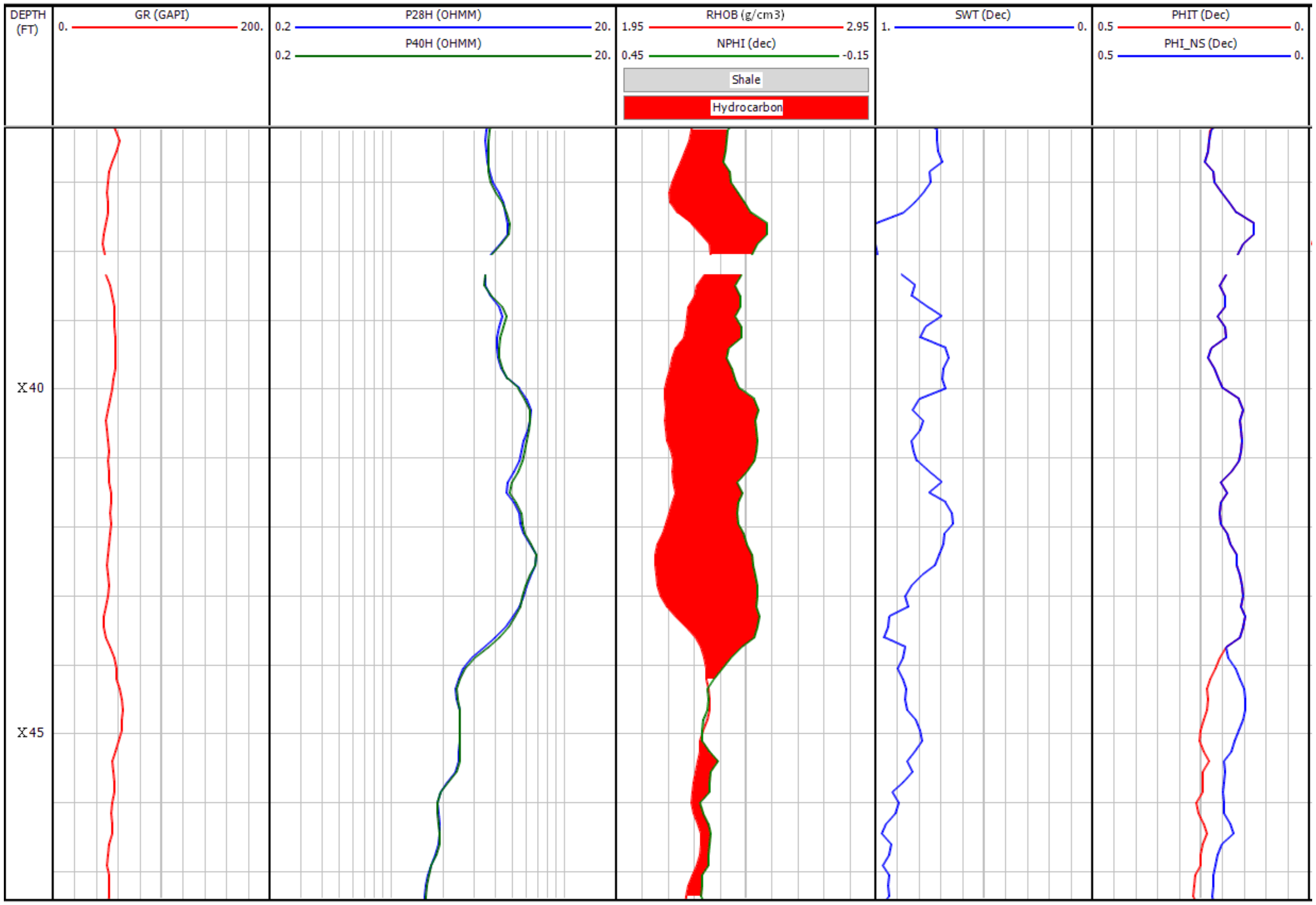

Figure 6.2: Field Case No. 3: LWD logs along the depth interval of interest. Track 1: depth. Track 2: gamma-ray log. Track 3: LWD apparent resistivity logs. Track 4: LWD nuclear logs (neutron porosity is calibrated in limestone porosity units). Track 5: total water saturation obtained from Archie's equation. Track 6: total porosity and non-shale porosity calculated with conventional interpretation.

Archie's Parameters	Symbol, Units	Value
Tortuosity Factor	a,[]	1
Cementation Exponent	m, []	1.87
Saturation Exponent	n, []	1.95
Connate-Water Resistivity (at 120.2 °F)	R_w, ohm.m	0.13

Table 6.3: Field Case No. 3: Archie's equation parameters used for calculation of water saturation.

The depth interval of interest is a layer with low gamma-ray log value, which exhibits a prominent cross-over between density and neutron porosity logs (calibrated in limestone porosity units) and relatively high apparent resistivity. Such a behavior could indicate presence of gas. **Figure 6.3** describes the agreement between available well logs and their numerical simulation obtained from the CSF. Simulation of nuclear logs indicates that the formation predominantly consists of sandstone matrix with approximately 14% illite. Total porosity calculated with the CSF is 18.5%, which is in good agreement with the total porosity of 17.92% calculated from NMR measurements. Total water saturation calculated with the CSF is 82%, which indicates that water is the dominant fluid in the pore space with the remainder being mostly residual gas. This result confirms that the cross-over exhibited by the density and neutron porosity logs is due to the presence of residual gas whereby the depth interval under consideration is not expected to produce hydrocarbons.

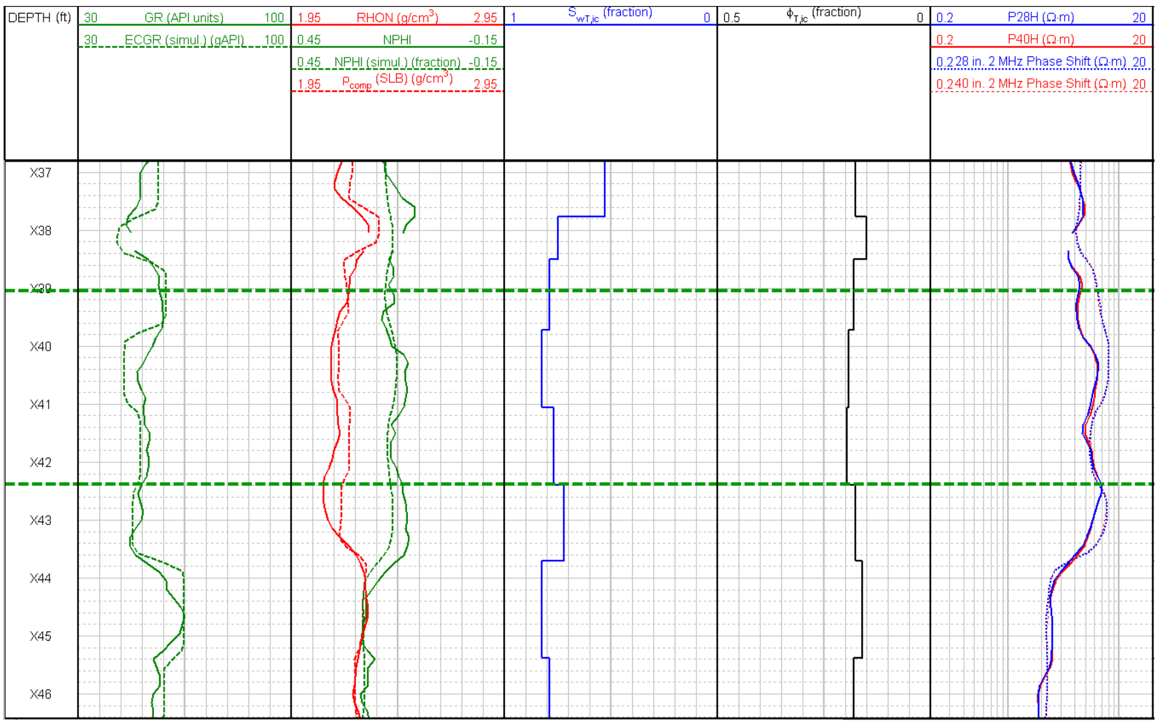

Figure 6.3: Field Case No. 3: Agreement between well logs and their numerical simulation obtained from the CSF. Solid lines identify measured logs while dashed lines identify simulated logs. Track 1: depth. Track 2: gamma-ray log. Track 3: nuclear logs (neutron porosity is calibrated in limestone porosity units). Track 4: layer-by-layer estimation of total S_w. Track 5: layer-by-layer estimation of total porosity. Track 6: LWD apparent resistivity logs. Only the interval included between the two horizontal green lines was considered for numerical simulation.

The T_2-D map calculated from 2D NMR measurements exhibits a strong gas signature which falsely leads one to believe that this could be an invaded formation with significant gas saturation, as was the case with Field Cases No. 1 and 2. However, fluid saturation estimation from the CSF indicated that the prominent gas signature observed on the T_2-D map was due to high residual gas saturation of 18%. Water saturation calculated for this depth interval was approximately 82%.

6.4 UNCERTAINTY ANALYSIS

Synthetic Gaussian noise is added to the borehole NMR measurements to quantify uncertainty in the estimation of both T_2-D map and T_2 distribution. **Figures 6.4** and **6.5** describe the T_2-D uncertainty map and the T_2 uncertainty bars, respectively, obtained by adding 20% normally distributed random noise to the data. **Figure 6.4** shows that in this field example the gas signature exhibits the maximum uncertainty, followed by the signature for mobile water. Compared to Field Cases No. 1 and 2, **Figure 6.5** indicates smaller uncertainty bars for the T_2 distribution even after adding a higher percentage of noise to the data. Such a behavior is attributed to the fact that the T_2-D NMR map for this field case was obtained by inverting a significantly larger number of echo-decay trains, thereby making the inversion more robust. Adding 5% Gaussian noise to the data yielded results with negligible uncertainty bars. Calculation of total porosity from borehole NMR measurements yielded a value of 17.92%. However, after adding 20% synthetic Gaussian noise, calculations for total porosity varied between 17.49% and 18.35% for the 200 noise realizations, which gives rise to a maximum variation of approximately 2.47%.

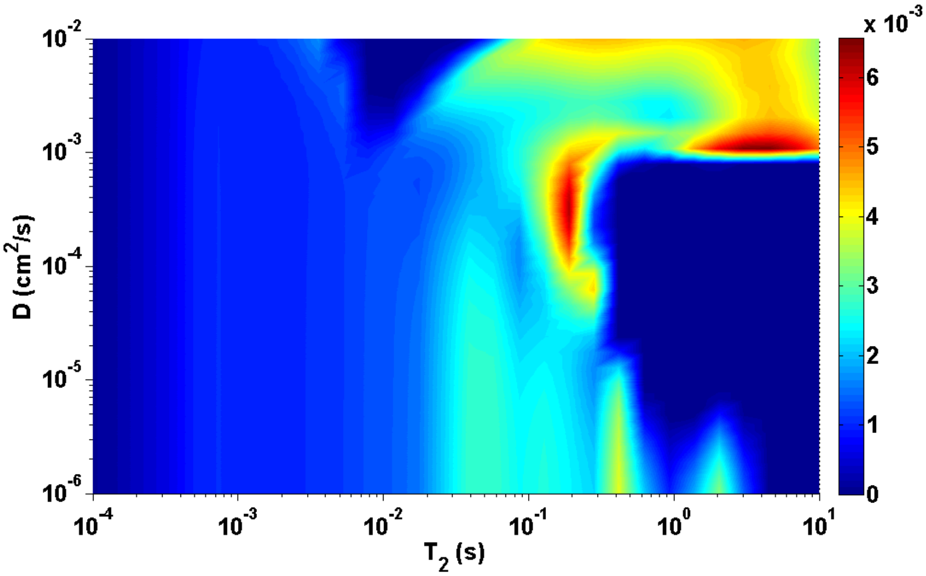

Figure 6.4: Field Case No. 3: T_2-D uncertainty map calculated by adding 20% Gaussian synthetic noise to the field data. Uncertainty is maximum at T_2 values corresponding to locations for fluid signatures of mobile water and gas. The color bar to the right describes porosity in percentage.

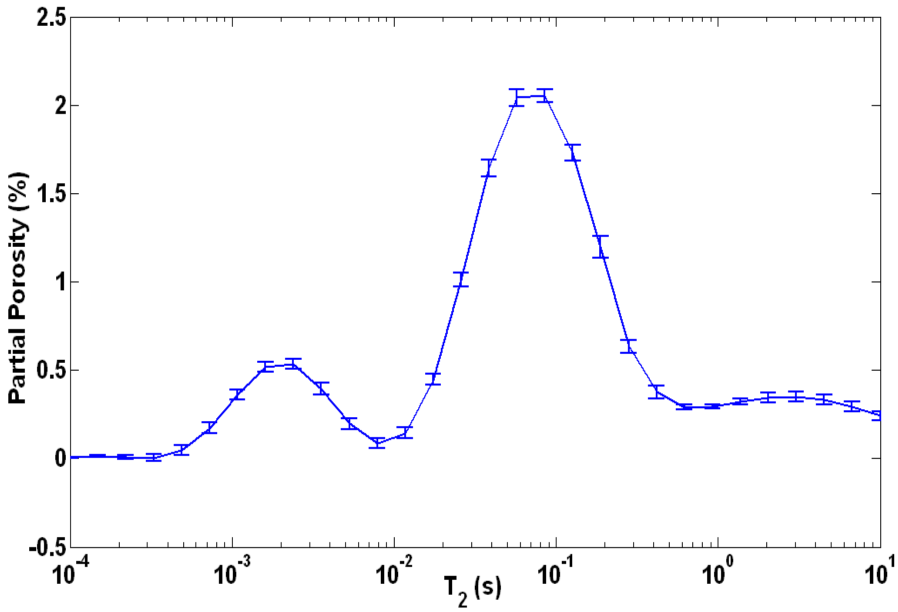

Figure 6.5: Field Case No. 3: Uncertainty bars of the T_2 distribution estimated by adding 20% Gaussian synthetic noise to the data.

Chapter 7: Summary and Conclusions

This section summarizes the workflow adopted for reconciliation of 2D NMR interpretations with the process of mud-filtrate invasion. The summary emphasizes the importance of combining petrophysical interpretations performed from 2D NMR inversion results with simulations of mud-filtrate invasion when estimating petrophysical properties of porous and permeable formations.

7.1 SUMMARY

An inversion algorithm in two dimensions for the estimation of partial porosity maps was introduced and developed in this thesis. Two-dimensional NMR maps were used for in-situ fluid identification and calculation of total and partial porosity. Uncertainty maps were generated to appraise the effect of adding synthetic noise to NMR measurements and to verify the robustness of the inversion algorithm.

For estimation of 2D NMR maps, this study relied on NMR data acquired with a specific radial length of investigation. Therefore, it was uncertain whether fluids diagnosed from 2D NMR maps, particularly hydrocarbon, were mobile or residual. It was determined that a reliable method to ascertain mobility of hydrocarbons was the numerical simulation of the process of mud-filtrate invasion.

For Field Cases No. 1 and 2, separation between apparent resistivity logs was observed due to radial variations of water saturation originating from the presence of a moving water-base mud-filtrate invasion front. This was confirmed when multi-layer static and dynamic petrophysical models were constructed via the CSF to numerically simulate the process of mud-filtrate invasion. Results provided insight to the radial distribution of fluids in the formation and enabled the accurate quantification of saturations for mobile hydrocarbon, residual hydrocarbon, and irreducible water. In Field Case No. 3, LWD apparent resistivity logs exhibited no separation, thus indicating that invasion was negligible.

Reconciliation of NMR measurements with the process of mud-filtrate invasion by numerical simulation of well logs was the most critical step of the analysis. NMR measurements exhibit a shallow radial length of investigation (approximately 6-10 in). Depth intervals selected for Field Cases No. 1 and 2 were predominantly hydrocarbon-bearing zones. However, petrophysical interpretations performed with the 2D NMR maps indicated that water was the dominant fluid while hydrocarbon exhibited a relatively weak signature. For Field Cases Nos. 1 and 2, 2D NMR interpretations were reconciled with the radial distribution of fluid saturation obtained from the CSF, whereby it was concluded that the NMR measurements were sensitive to a radial zone which exhibited hydrocarbon saturation approximately equal to residual hydrocarbon saturation and that most of existing mobile hydrocarbon components had been displaced by the invading mud-filtrate.

In Field Case No. 1, petrophysical interpretations obtained with the CSF indicated presence of isolated porosity. The CSF could differentiate between total, interconnected, and isolated porosity while 2D NMR maps inferred total porosity. In Field Case No. 2, borehole NMR data were biased because of internal magnetic field gradients due to presence of pyrite and chlorite. Total porosity evaluated from NMR data was biased and significantly higher than porosity reported from both core analysis and the CSF. For Field Case No. 3, the estimated T_2-D map exhibited a relatively strong gas signature, suggesting a hydrocarbon-bearing interval. However, reconciliation of NMR interpretations with the CSF revealed that water was the dominant fluid and that gas was at a stage of residual saturation. The above field examples provided compelling evidence that reconciliation of NMR measurements with mud-filtrate invasion is essential to estimate accurate and reliable petrophysical properties.

7.2 CONCLUSIONS

The items below summarize the most important conclusions stemming from this thesis:

(1) Inversion of NMR measurements in two dimensions provides detailed and discriminatory information about petrophysical properties and saturating fluids when compared to conventional 1D inversion techniques. Using 2D NMR inversion enables better identification of individual fluid signatures and yields more accurate calculations of partial fluid porosity than 1D NMR inversion.

(2) NMR measurements exhibit a shallow radial length of investigation. Consequently, in field cases exhibiting moderate to deep invasion, the NMR response of virgin reservoir fluids is often masked by drilling fluids because of the processes of mud-filtrate invasion, fluid displacement, and mixing.

(3) In formations invaded by water-base mud filtrate (Field Cases No. 1 and 2), conventional fluid identification methods using apparent resistivity logs indicate predominantly water within the flushed zone. Two-dimensional NMR interpretations indicate presence of multiple fluids which may include mobile water, mud filtrate, hydrocarbon, and clay-bound and capillary-bound water. It is important to ascertain whether existing hydrocarbons are residual or mobile using petrophysical interpretation techniques which can estimate radial distributions of hydrocarbon saturation.

(4) A reliable and accurate method to approach the problem indicated in the previous item is the reconciliation of NMR measurements with the process of mud-filtrate invasion. This is done by constructing multi-layered static and dynamic models and performing numerical simulations of mud-filtrate invasion to honor available apparent resistivity and nuclear logs.

(5) Numerical simulation of the process of mud-filtrate invasion yields quantitative estimations of the radial distribution of fluid saturations. By reconciling this information with calculation of fluid saturation performed with 2D NMR data, estimations can be made of the approximate "radial zone of response" of NMR measurements.

(6) As emphasized by the field examples considered in this thesis, NMR measurements alone do not provide complete and conclusive petrophysical interpretation. For example, in Field Case No. 1, presence of isolated porosity was not detected by NMR measurements. In Field Case No. 2, porosity measurements obtained from NMR data were biased while in Field Case No. 3, NMR measurements could not ascertain that hydrocarbon saturation was residual and that mobile hydrocarbon saturation was negligible.

(7) Uncertainty analysis performed by adding synthetic Gaussian noise to the acquired borehole NMR data indicated that maximum uncertainty occurs at fluid-signature peaks; T_2 values in the vicinity of clay-bound and capillary-bound water were also susceptible to high uncertainty. Field Case No. 3 indicated that uncertainty in NMR inversion results can be reduced by adopting a robust data acquisition strategy, which may include a wide range of values for acquisition parameters such as *TW*, *TE*, *G*, and *NE*. An important observation is that, despite

adding synthetic noise, locations of peaks for fluid signatures remained constant and that no other abnormal behavior was observed on estimated 2D NMR maps.

Appendix A: Rock Classification

A.1 Winland's Rock Classification Method

H. D. Winland developed an empirical relationship among porosity, permeability, and pore-throat size corresponding to different air-mercury saturations. He classified petrophysical formations on the basis of their storage and flow capacities inferred from core measurements (Pittman, 1992). Winland's experiments considered 82 core samples (56 sandstone samples and 26 carbonate samples) with low permeability samples corrected for gas slippage, also known as Klinkenberg correction (Klinkenberg, 1941). He performed regression analysis for different saturations of mercury injection and found that the correlation that corresponded to 35% of mercury saturation yielded the best approximation for permeability given total porosity and pore-throat radius. The regression equation advanced by Winland is given by

$$Log_{10}\left(r_{35}\right) = 0.732 + 0.588 \cdot Log_{10}\left(k_{air}\right) - 0.864 \cdot Log_{10}\left(\phi_t\right), \tag{A1}$$

where r_{35} is pore-throat radius in μm corresponding to the 35th percentile of mercury saturation in a mercury porosimetry test, k_{air} is the permeability of sample saturated with air expressed in md, and ϕ_t represents total porosity in percentage. For Field Cases No. 1 and 2, available core data included total porosity and permeability measurements.

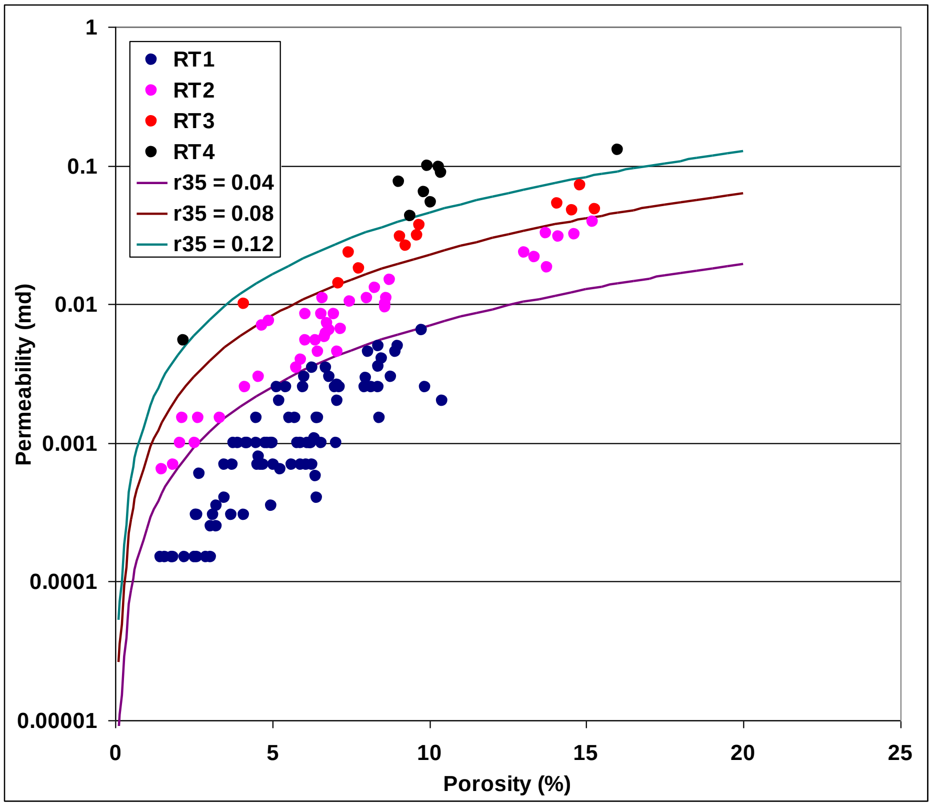

Figure A.1: Four distinct flow units identified from Winland's (r_{35}) rock classification method (RT1, RT2, RT3, and RT4). The variable r_{35} is given in µm.

Figure A.1 shows results obtained from Winland's rock classification method, emphasizing four distinct flow units. A fifth rock type described as shale was added to the four rock types based on a lower limit for volumetric concentration of shale, determined jointly from gamma-ray and nuclear logs to be equal to 65%.

Appendix B: Pore-Level NMR Framework

This Appendix describes the application of a general pore-scale framework, developed by Toumelin et al. (2004), to simulate suites of NMR data in complex rock models. The pore-scale framework implements random-walk simulations of NMR incorporating multiphase fluid diffusion, and T_1 and T_2 relaxations. From equations (1.1) and (1.2), it follows that the NMR response of a formation is influenced by the magnetic properties of saturating fluids and their spatial distribution in the pore space. Therefore, a pore-level investigation of petrophysical properties of grain packs is useful to understand the sensitivity of NMR measurements to fluid and petrophysical properties.

The objective pursued in this appendix is to validate 2D NMR results obtained from borehole NMR measurements for Field Case No. 1 by performing pore-level NMR simulations to generate saturation-dependent T_1-T_2 maps from a synthetically generated grain pack. To that end, the synthetic grain pack is constructed such that it closely reproduces the properties of the formation described in Field Case No. 1, namely porosity, fluid distribution, fluid magnetic properties, grain size distribution, compaction and internal layering effects.

B.1 Overview

Core and pore-scale laboratory analyses report that the depth interval discussed in Field Case No. 1 exhibits a bimodal grain-size distribution. As mentioned in Section 4.1, geologic information indicates that the formation is a laminated and cross-laminated transgressive-regressive sequence exhibiting thin layers. In order to appropriately represent internal layering effects exhibited by the formation, a synthetic bilayered grain pack was constructed for pore-level NMR simulations. After its construction, the grain pack was digitized and a fluid percolation algorithm was implemented to saturate it with two immiscible fluids. The percolation algorithm yielded several digitized packs, with a wide range of S_w values. Subsequently, pore-level NMR simulations were applied to the digitized grain packs and processed with the 2D NMR inversion algorithm to generate saturation-dependent T_1-T_2 maps. These results were then analyzed and reconciled with the field 2D NMR map (**Figure 4.1**) to cross-validate results obtained from simulation of water-base mud-filtrate invasion. The following sections provide a concise description of each step implemented in the cross-validation effort.

B.2 CONSTRUCTION AND DIGITIZATION OF GRAIN PACK

Petrographic thin-section analysis indicates that the formation in this depth interval exhibits a bimodal grain-size distribution, with the grain radii of the two modes being approximately equal to 5 μm and 100 μm, respectively. To keep the analysis simple but realistic, spherical grains were assumed and two separate grain packs were constructed with grain radii of 5 μm and 100 μm each, respectively. These two grain packs were then stacked to produce a composite, bilayered grain pack. As mentioned in Section B.1, a bilayered pack was required to appropriately represent internal layering effects inherent to a cross-laminated depositional environment.

An algorithm based on random sequential deposition of grains was implemented for the construction of a grain pack (Coelho et al., 1997). Accordingly, while being deposited, each grain performed a local search, horizontally and vertically, seeking a position with the lowest potential energy. Once deposited, the grain is considered to be stationary. In other words, the final position of a settled grain is determined by the configurations of previously deposited grains. Since the upper Almond formation is naturally compacted, exhibiting high overburden pressure, it is important to simulate the process of grain compaction when constructing a geologically consistent grain pack. Spherical grain packs, if not compacted, generally yield porosity values in excess of 35%. Therefore, to obtain the desired porosity (below 15%) for this tight-gas formation, grain compaction was included in the generation of the grain pack. Compaction under overburden stress was modeled by the combined effects of maximum overlap allowed between grains and the number of iterations allowed for each grain to find the position of lowest potential energy.

Figures B.1 and **B.2** show a slice along the *x-y* plane of the spherical grain packs with grain radii 100 μm and 5 μm, respectively. Grain packs are cubic with a side length of 250 μm. In these figures, grains are identified with gray and pore space is identified with black, while overlap between neighboring grains, which represents grain compaction, is identified with white. Total porosity of the grain pack with grain radii equal to 100 μm is approximately 12.53% and is constructed with 26 grains, while the total porosity of the grain pack with grain radii equal to 5 μm is approximately 14.11% and is constructed with 233,179 grains. Total porosity of the combined, bilayered grain pack is 13.32%.

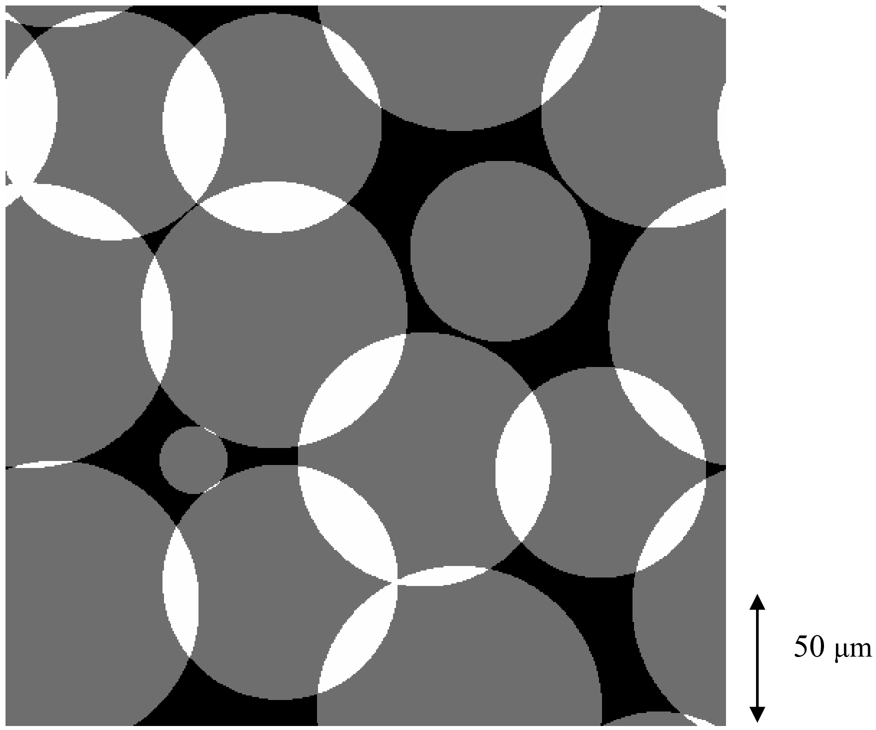

Figure B.1: Slice along the *x-y* plane of a cubic grain pack with side length of 250 μm and grain radii equal to100 μm. Grains and pores are identified with gray and black, respectively, while overlap between neighboring grains, representing grain compaction, is identified with white. The pack was constructed with 26 grains and it exhibits a porosity of 12.53%.

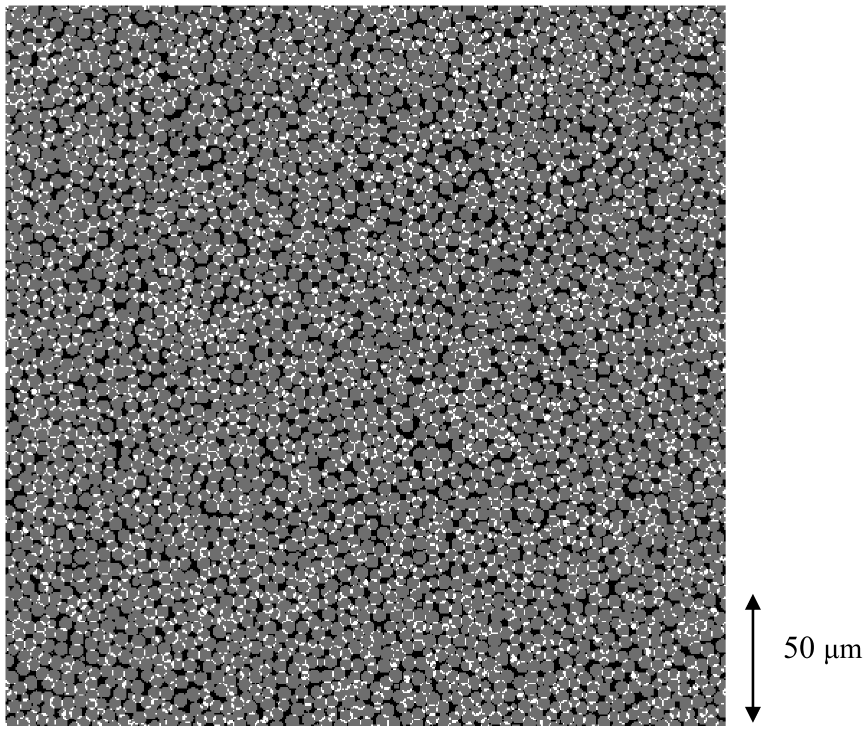

Figure B.2: Slice along the *x-y* plane of a cubic grain pack with side length of 250 μm and grain radii equal to 5 μm. Grains and pores are identified with gray and black respectively, while overlap with neighboring grains, representing grain compaction, is identified with white. The pack was constructed with 233,179 grains and it exhibits a porosity of 14.11%.

After its construction, the bilayered grain pack with the desired porosity was digitized (discretized) into voxels to be subsequently used as input for percolation and NMR simulations. A voxel is the smallest unit of the digitized grain pack. It is essential that a suitable voxel size be used so that grains and pores are approximated with sufficient spatial resolution to yield accurate percolation and NMR simulations. As a guideline, voxel size should be at least five times smaller than the smallest grain radius. For the work described in this thesis, a voxel size of 1 μm was used to describe both spherical grain packs. The voxelization algorithm considers only solid grains as grain type and cannot take into account microporosity due to grain-coating clay, for instance.

B.3 DETERMINATION OF THE SPATIAL DISTRIBUTION OF IMMISCIBLE FLUIDS

Percolation simulation determines the spatial distribution of two immiscible fluids in the pore space of a digitized spherical grain pack. The percolation algorithm is based on the concept of maximal inscribed spheres (Silin et al., 2003). While executing the percolation algorithm, a distribution of maximal inscribed spheres is obtained, which is used to synthetically simulate a mercury injection porosimetry experiment. Such an experiment yields a saturation-dependent dimensionless capillary pressure curve.

The percolation algorithm was applied to the bilayered grain pack to generate several digitized grain packs. Each of these digitized grain packs represented a different saturation and spatial distribution of two immiscible fluids and a corresponding dimensionless capillary pressure. Water was assumed to be the wetting fluid phase in all the simulations. Results obtained from the percolation algorithm applied to the bilayered spherical grain pack were consistent with laws of capillary pressure in porous media. At high values of water saturation, it was observed that pore space attributed to the 5 μm grains was completely saturated with the wetting phase and that only larger pores included the non-wetting phase. However, at low values of water saturation, the non-wetting phase was present throughout the pore space.

Figure B.3 shows the digitized and concatenated grain pack, with 100% water saturation, rendered by the percolation simulation. The figure shows a slice of the concatenated grain pack along the *x-z* plane. Fluid percolation simulations were performed using the Pore-Level Petrophysics Module (PLPM[5]) of UTAPWeLS. Grains are identified with yellow, whereas water is identified with blue. **Figure B.4** shows a similar image with 46% water saturation. In this latter figure, most of the non-wetting phase (gas), identified with red, is contained in the large pores within the upper half of the grain pack. Smaller-size pores in the lower half of the grain pack are predominantly saturated with water and a trace of gas.

[5] Developed by The University of Texas at Austin's Research Consortium on Formation Evaluation.

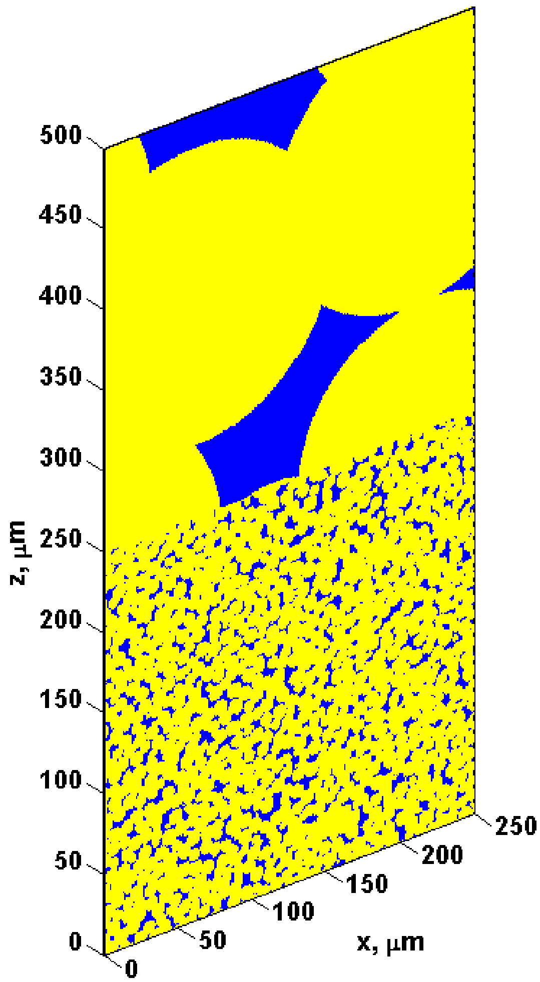

Figure B.3: Digitized image of the bilayered grain pack with S_w equal to 100%, obtained after performing the percolation simulation. The figure shows a slice of the grain pack along the *x*-*z* plane. Grains are identified with yellow whereas water (which is the wetting phase) is identified with blue.

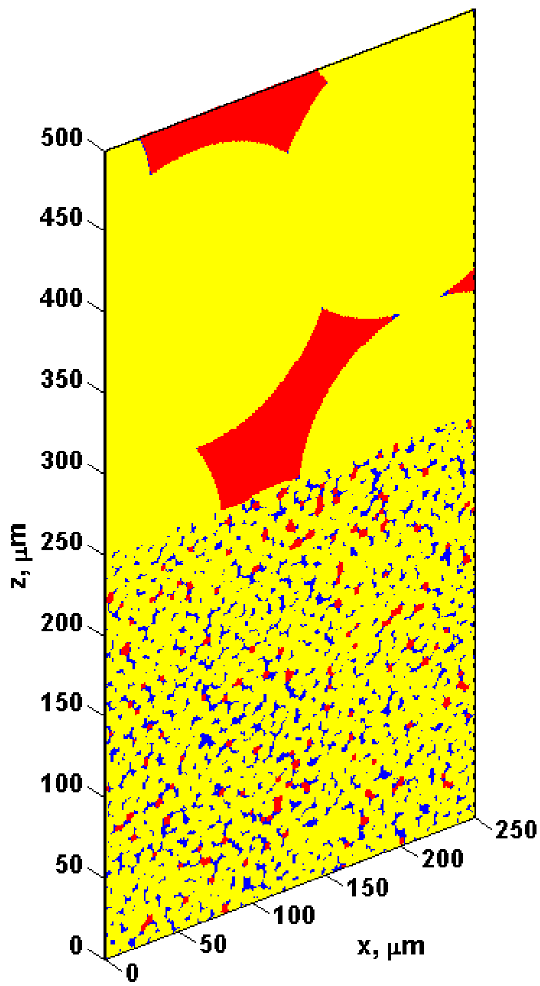

Figure B.4: Digitized image of the bilayered grain pack with S_w equal to 46%, obtained after performing the percolation simulation. The figure shows a slice of the grain pack along the *x-z* plane. Grains are identified with yellow, while water and gas are identified with blue and red, respectively. Gas is mostly located in the large-size pores whereas small pores are predominantly saturated with water.

B.4 Pore-Level NMR Simulations

The NMR response of porous rocks was simulated using a three-dimensional random-walk algorithm which solves Bloch-Torrey's equations along diffusion pathways of individual fluid molecules within the digitized spherical grain pack (Toumelin et al., 2004). For Field Case No 1, water saturation calculated from **Table 4.2** indicated that NMR measurements originated from a radial zone where S_w was approximately 85%. Consequently, the percolated pack with S_w value closest to 85% was selected for pore-level NMR simulations to generate suites of NMR data.

Table B.1 describes the fixed parameters used as inputs for all the pore-level NMR simulations. These parameters include T_{1B}, T_{2B}, D, ρ_1, and ρ_2 for the wetting and non-wetting phases, G, and number of random-walkers implemented in the simulation. A CPMG pulsed-sequence method was selected to simulate the NMR data. The 90^o and 180^o pulse durations were fixed at 30 μs and 20 μs, respectively. Information about G and the CPMG pulse sequence were obtained from available tool specifications and the assumed data acquisition strategy, respectively. Values for ρ_1 and ρ_2 for a sandstone formation with wetting and non-wetting phases were the same as those suggested by Toumelin et al. (2004), while approximate values of D, T_{1B}, and T_{2B} were selected for this field example based on laboratory measurements performed on fluid samples acquired in another well within the same field. To maintain consistency with Field Case No. 1, pore-level NMR simulations generated an echo-decay train for each set of acquisition parameters listed in **Table 4.1**, yielding a sequence comprising six echo-decay trains, which were subsequently processed using the 2D NMR inversion algorithm to obtain saturation-dependent T_1-T_2 maps.

Fluid	T_{1B} [s]	T_{2B} [s]	D [cm^2/s]	ρ_1 [μm/s]	ρ_2 [μm/s]	G [gauss/cm]	No. of Random Walkers []
Water	0.2	0.1	2x10^{-5}	20	35	16	500
Gas	2	0.3	0.1x10^{-5}	7	10		

Table B.1: Fluid magnetic properties, tool magnetic gradient and number of random walkers used as inputs to the pore-level NMR simulations to generate synthetic NMR measurements.

Pore-level NMR simulations were performed for the grain pack shown in **Figure B.5**, where S_w is equal to 87%. These NMR echo-decay data were then used as input to the 2D inversion algorithm to generate the T_1-T_2 map shown in **Figure B.6**. Three fluid signatures are diagnosed from the map: gas and invading water-base mud filtrate contained in large pores, and water-base mud filtrate and connate water contained in small pores. Signatures for clay-bound water and capillary-bound water are missing. When compared to the T_1-T_2 map obtained for Field Case No. 1, shown in **Figure 4.1**, the location and relative magnitudes for signatures of gas and water-base mud filtrate agree well.

These results confirm that NMR is a pore-level phenomenon and that NMR signals acquired and processed under field conditions can be simulated using pore-level techniques. Simulation results also verify that the assumption of a bilayered grain pack to represent internal layering effects for this depositional environment is appropriate because it reproduces field measurements. This exercise also validates the calculated water saturation of approximately 85% for the radial length of investigation of NMR measurements (Section 4.4).

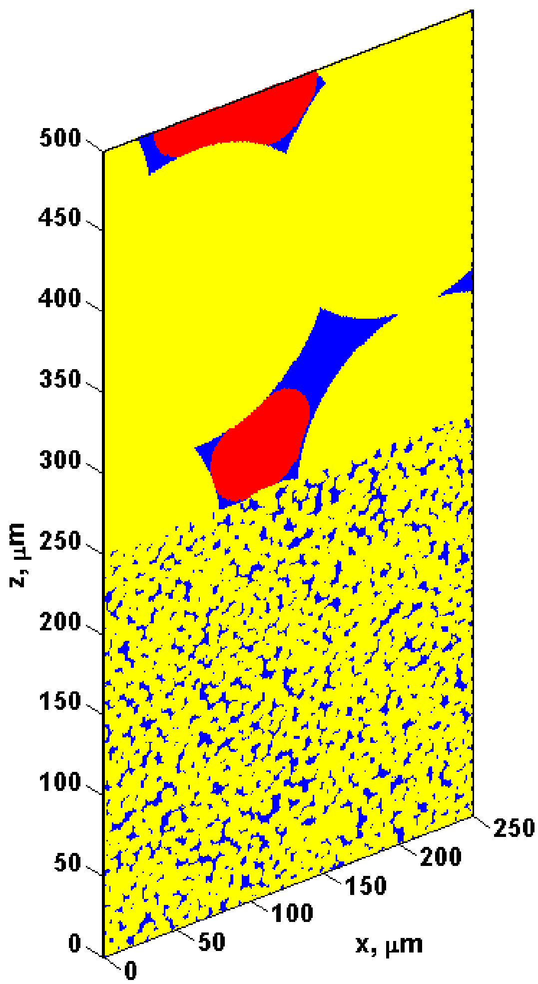

Figure B.5: Digitized image of the bilayered grain pack with S_w equal to 87%, obtained from the percolation simulation. The figure shows a slice of the grain pack along the *x-z* plane. Grains, water, and gas are identified with yellow, blue, and red, respectively. At low values of S_g, gas is located within large-size pores whereas small pores become completely saturated with water.

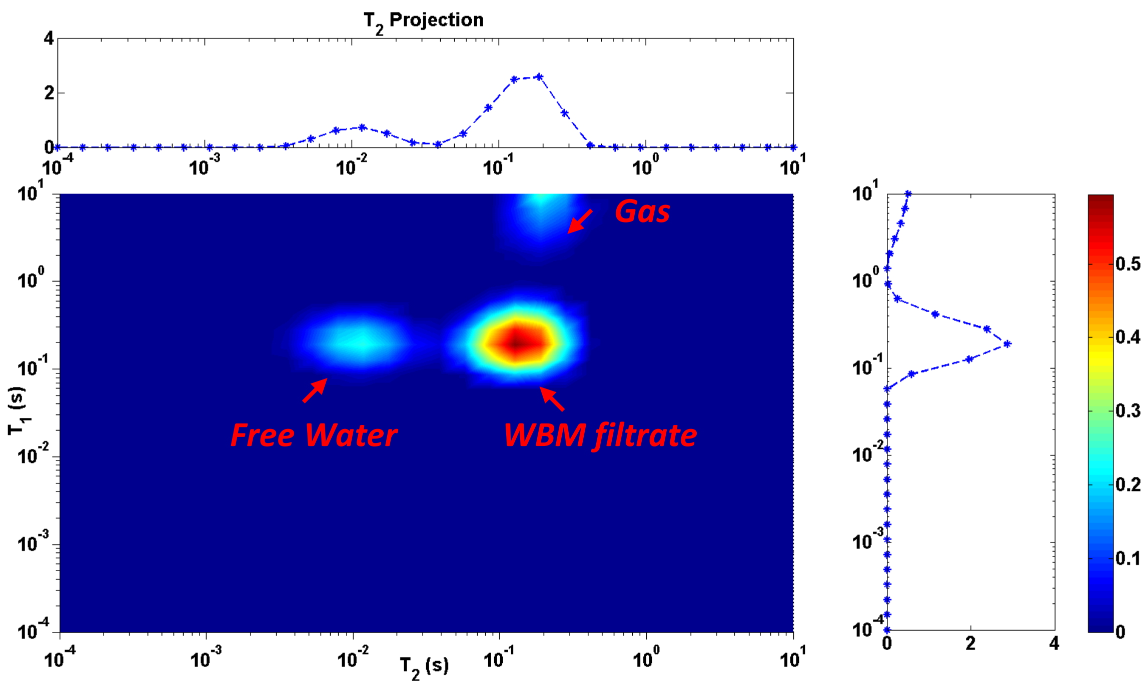

Figure B.6: T_1-T_2 map obtained for the bilayered grain pack shown in **Figure B.5**. Three distinct fluid signatures are diagnosed from the map: gas, water-base mud filtrate, and mobile water. Location and relative spread of observed fluid signatures are similar to those of the T_1-T_2 map obtained for Field Case No. 1. The color bar to the right describes porosity in percentage.

Nomenclature

T_1	:	Longitudinal relaxation time, [s]
T_2	:	Transverse relaxation time, [s]
TW	:	Wait time, [s]
TE	:	Inter-echo time, [s]
NE	:	Number of echoes, []
G	:	Magnetic field gradient, [gauss/cm]
D	:	Fluid diffusion coefficient, [cm^2/s]
T_{1B}	:	Bulk longitudinal relaxation time, [s]
T_{2B}	:	Bulk transverse relaxation time, [s]
S/V	:	Pore surface to volume ratio, [cm^{-1}]
γ	:	Gyromagnetic ratio for a hydrogen proton
ρ_1	:	Longitudinal surface relaxivity, [cm/s]
ρ_2	:	Transverse surface relaxivity, [cm/s]
R	:	Ratio of T_1 and T_2, []
$C(m)$	:	Cost function, []
$m(x,y)$	:	Two-dimensional model of variables x and y, []
F	:	Linear operator, []
d	:	Data, []
$\boldsymbol{W_d}$	:	Data-weighting matrix, []
$\boldsymbol{F}$	:	Discretized kernel matrix, []
$\boldsymbol{m}$	:	Model vector, []
$\boldsymbol{d}$	:	Data vector, []
λ	:	Regularization (stabilization) factor, []
$\boldsymbol{W_m}$	:	Model-weighting matrix, []
$\boldsymbol{I}$	:	Identity matrix, []

σ	:	Standard deviation, []
a	:	Archie's tortuosity factor, []
k	:	Permeability, [md]
m	:	Archie's cementation exponent, []
n	:	Archie's saturation exponent, []
t	:	Time, [s]
ϕ_t	:	Total porosity, [frac.]
ϕ_{ns}	:	Non-shale porosity, [frac.]
$\phi_{t,ic}$	:	Total interconnected porosity, [frac.]
S_{gr}	:	Residual gas saturation, [frac.]
R_w	:	Connate-water electrical resistivity, [ohm.m]
R_{mf}	:	Mud-filtrate electrical resistivity, [ohm.m]
C_w	:	Connate-water salinity, [ppm NaCl equivalent]
S_{wt}	:	Total connate-water saturation, [frac.]
S_{xo}	:	Flushed-zone water saturation, [frac.]
e_p	:	Pore-size distribution exponent, []
e_{nw}	:	Experimental exponent (non-wetting phase) for Brooks-Corey's equation, []
e_w	:	Experimental exponent (wetting phase) for Brooks-Corey's equation, []
S_{wr}	:	Residual wetting-phase saturation, [frac.]
P_c^0	:	Coefficient for Pc equation, [psi.darcy$^{1/2}$]
k^0_{rnw}	:	k_{rnw} (non-wetting phase) end point, []
k^0_{rw}	:	k_{rw} (wetting phase) end point, []

Acronyms

1D	:	One-Dimensional
2D	:	Two-Dimensional
NMR	:	Nuclear Magnetic Resonance
DC	:	Direct Current
CSF	:	Common Stratigraphic Framework
dB	:	Decibel
UTAPWeLS	:	The University of Texas at Austin's Petrophysical and Well-Log Simulator
CPMG	:	Carr-Purcell-Meiboom-Gill
PLPM	:	Pore-Level Petrophysics Module of UTAPWeLS
IFK	:	Fredholm Integral Equation of the First Kind
MMCFD	:	Million Cubic Feet per Day
ppm	:	Parts Per Million
LWD	:	Logging-While-Drilling
STP	:	Standard Temperature and Pressure
SNR	:	Signal-To-Noise Ratio

References

Aster, R., Borchers, B., and Thurber, C., 2005, Parameter Estimation and Inverse Problems: Elsevier Academic Press, Burlington, Massachusetts.

Brooks, R.H. and Corey, A.J., 1964, Hydraulic Properties of Porous Media: Hydrology Papers, Colorado State University, Fort Collins, Colorado.

Chen, S., Shao, W., Hursan, G., and Sun, B., 2009, Improvement of NMR multi-dimensional inversion methods for accurate petrophysical and fluid quantification analyses: Paper GGGG, *Transactions of the SPWLA 50th Annual Logging Symposium*, The Woodlands, Texas, June 21-24.

Coates, G. R., Vinegar, H. J., Tutunjian, P. N., and Gardner, J. S., 1993, Restrictive diffusion from uniform gradient NMR well logging: SPE 26472, *Proceedings of the SPE Annual Technical Conference and Exhibition*: Society of Petroleum Engineers, Houston, Texas, October 3-6.

Coelho, D., Thovert, J. F., and Adler, P. M., 1997, Geometrical and transport properties of random packings of spheres and aspherical particles: *Physical Review E*, vol. 55, no. 2, pp. 1959-1978.

Dunn, K. and LaTorraca, G., 1999, The inversion of NMR data sets with different measurement errors: *Journal of Magnetic Resonance*, vol. 140, no. 1, pp. 153-161.

Fukushima, E. and Roeder, S. B. W., 1981, Experimental Pulse NMR: A Nuts and Bolts Approach: Addison-Wesley, Reading, Massachusetts.

Gandhi, A., Torres-Verdín, C., Voss, B., Gabulle, J., and Seminario, F., 2010, Construction of reliable static and dynamic multi-layer petrophysical models in Camisea gas reservoirs, Peru: Paper CC, *Transactions of the SPWLA 51th Annual Logging Symposium*, Perth, Australia, June 19-23.

Hansen, P. C., 2007, Regularization Tools: A Matlab package for analysis and solution of discrete ill-posed problems: *Numerical Algorithms*, vol. 46, no. 2, pp. 189-194.

Kenyon, W. E., 1997, Petrophysical principles of applications of NMR logging: *The Log Analyst*, vol. 38, no. 2, pp. 21-43.

Klinkenberg, L. J, 1941, The permeability of porous media to liquids and gases: *Drilling and Production Practices*, American Petroleum Institute, pp. 200-213.

Pittman, E. D., 1992, Relationship of porosity and permeability to various parameters derived from mercury injection capillary pressure curves for sandstones: *AAPG Bulletin*, vol. 76, no. 2, pp. 191-198.

Silin D., Jin, G., and Patzek, T., 2003, Robust determination of the pore space morphology in sedimentary rocks: SPE 84296, *Proceedings of the SPE Annual Technical Conference and Exhibition*: Society of Petroleum Engineers, Denver, Colorado, October 5-8.

Sun, B. and Dunn, K. J., 2005, Two-dimensional nuclear magnetic resonance petrophysics: *Journal of Magnetic Resonance Imaging*, vol. 23, Issue 2, pp. 259-262.

Shafer, J., Chen, J., Flaum, M., Hirasaki, G., Boyd, A., Straley, C., Borbas, T., and Devier, C., 2004, Core and log NMR measurements indicate reservoir rock is altered by OBM filtrate: Paper CC, *Transactions of the SPWLA 45th Annual Logging Symposium,* Noordwijk, The Netherlands, June 6-9.

Tobin, R. C., McClain, T., Lieber, R. B., Ozkan, A., Banfield, L. A., Marchand, A. M. E., and McRae, L. E., 2010, Reservoir quality modeling of tight-gas sands in Wamsutter field: integration of diagenesis, petroleum systems, and production data: *AAPG Bulletin*, vol. 94, no. 8, pp. 1229-1266.

Toumelin, E., Torres-Verdín, C., Sun, B., and Dunn, K., 2004, A numerical assessment of modern borehole NMR interpretation techniques: SPE 90539, *Proceedings of the SPE Annual Technical Conference and Exhibition*: Society of Petroleum Engineers, Houston, Texas, September 26-29.

Voss, B., Torres-Verdín, C., Gandhi, A., Alabi, G., and Lemkecher, M., 2009, Common stratigraphic framework to simulate well logs and to cross-validate static and dynamic petrophysical interpretations: Paper PPP, *Transactions of the SPWLA 50th Annual Logging Symposium*, The Woodlands, Texas, June 21-24.

Vita

Kanay Jerath was born in the "City Beautiful" of Chandigarh, India, on July 17, 1985. After finishing his high school education from St. John's High School, Chandigarh, he joined Netaji Subhas Institute of Technology, University of Delhi in 2004 to pursue a B.E. degree in Instrumentation and Control Engineering. In summer 2007, he interned at the University of Western Australia, Perth. Between June 2009 and August 2011, Kanay was a graduate research assistant with the Formation Evaluation Group in the Department of Petroleum and Geosystems Engineering of The University of Texas at Austin. In summer 2010 he interned with Anadarko Petroleum Corporation in The Woodlands, TX. Upon completion of his Master's degree, Kanay will return to Anadarko's Petrophysical Technology group as a Petrophysicist.

Permanent address:

House No. 1481, Sector 21

Panchkula, Haryana

India – 134112

Permanent e-mail address:

kanayjerath@gmail.com

This thesis was typed by the author.